

# Decadal trends in global CO emissions as seen by MOPITT

Yi Yin<sup>1</sup>, Frédéric Chevallier<sup>1</sup>, Philippe Ciais<sup>1</sup>, Grégoire Broquet<sup>1</sup>, Audrey Fortems-Cheiney<sup>2</sup>,  
Isabelle Pison<sup>1</sup>, Marielle Saunois<sup>1</sup>

5 <sup>1</sup>Laboratoire des Sciences du Climat et de l'Environnement, CEA-CNRS-UVSQ, UMR8212,  
Gif-sur-Yvette, France

<sup>2</sup>Laboratoire Interuniversitaire des Systèmes Atmosphériques, CNRS/INSU, UMR7583,  
Université Paris-Est Créteil et Université Paris Diderot, Institut Pierre Simon Laplace, Créteil,  
France

10

## Abstract

Negative trends of carbon monoxide (CO) concentrations are observed in the recent decade  
by both surface measurements and satellite retrievals over many regions of the globe, but  
they are not well explained by current emission inventories. Here, we attribute the observed  
15 CO concentration decline with an atmospheric inversion that simultaneously optimizes the  
two main CO sources (surface emissions and atmospheric hydrocarbon oxidations) and the  
main CO sink (atmospheric hydroxyl radical OH oxidation) by assimilating observations of  
CO and of chemically related tracers. Satellite CO column retrievals from Measurements of  
Pollution in the Troposphere (MOPITT), version 6, and surface observations of methane and  
20 methyl-chloroform mole fractions are assimilated jointly for the period covering 2002-2011.  
Compared to the model simulation prescribed with prior emission inventories, trends in the  
optimized CO concentrations show better agreement with that of independent surface in-situ  
measurements. At the global scale, the atmospheric inversion primarily interprets the CO  
concentration decline as a decrease in the CO emissions ( $-2.3\% \text{ yr}^{-1}$ ), more than twice the  
25 negative trend estimated by the prior emission inventories ( $-1.0\% \text{ yr}^{-1}$ ). The spatial  
distribution of the inferred decrease of CO emissions indicates contributions from West  
Europe ( $-4.0\% \text{ yr}^{-1}$ ), United States ( $-4.6\% \text{ yr}^{-1}$ ) and East Asia ( $-1.2\% \text{ yr}^{-1}$ ) where  
anthropogenic fuel combustion generally dominates the overall CO emissions, and also from

30 Australia ( $-5.3\% \text{ yr}^{-1}$ ), the Indo-China Peninsula ( $-5.6\% \text{ yr}^{-1}$ ), Indonesia ( $-6.7\% \text{ yr}^{-1}$ ), and  
South America ( $-3\% \text{ yr}^{-1}$ ) where CO emissions are mostly due to biomass burning. In  
contradiction with the bottom-up inventories that report an increase of  $2\% \text{ yr}^{-1}$  over China  
during the study period, a significant emission decrease of  $1.1\% \text{ yr}^{-1}$  is inferred by the  
inversion. A large decrease in CO emission factors due to technology improvements would  
outweigh the increase of carbon fuel combustions and may explain this decrease. Independent  
35 satellite formaldehyde ( $\text{CH}_2\text{O}$ ) column retrievals confirm the absence of large-scale trends in  
the atmospheric source of CO. However, the  $\text{CH}_2\text{O}$  retrievals are not assimilated and OH  
concentrations are optimized at very large scale in this study. Future studies could investigate  
potential sub-regional trends in the atmospheric sources of CO or in the OH concentrations,  
and thus further refine the estimation of regional CO emissions and associated trends.

40

## 1 Introduction

Carbon monoxide (CO) is an air pollutant that leads to the formation of tropospheric ozone (O<sub>3</sub>) and carbon dioxide (CO<sub>2</sub>) (Jacob, 1999). It is the major sink of the tropospheric oxidant hydroxyl radical (OH), and hence influences concentrations of methane (CH<sub>4</sub>) and non-methane volatile organic compounds (NMVOCs) (Logan *et al.*, 1981). It contributes to an indirect positive radiative forcing of  $0.23 \pm 0.07 \text{ Wm}^{-2}$  at the global scale (Stocker *et al.*, 2013). Atmospheric CO has two main sources: (i) direct surface CO emissions from fuel combustion and biomass burning, estimated to be  $\sim 500\text{-}600 \text{ TgCO yr}^{-1}$  and  $\sim 300\text{-}600 \text{ TgCO yr}^{-1}$ , respectively, by emission inventories (Granier *et al.*, 2011 and references herein), and (ii) secondary chemical oxidation of hydrocarbons in the troposphere, estimated to be a source of  $\sim 1200\text{-}1650 \text{ TgCO yr}^{-1}$  with considerable differences among studies (Holloway *et al.*, 2000; Pétron *et al.*, 2004; Shindell *et al.*, 2006; Duncan and Logan, 2008). The sink of CO is mainly through oxidation by OH (Logan *et al.*, 1981), which defines an average lifetime of 2 months for CO in the atmosphere.

Surface in-situ measurements in Europe (Zellweger *et al.*, 2009; Angelbratt *et al.*, 2011), over the USA (Novelli *et al.*, 2003; EPA, 2011), in some large cities in China (Li and Liu, 2011), and in many other places (Yoon and Pozzer, 2014) indicate that CO concentrations have been decreasing for more than ten years. Negative trends have also been observed by various satellite sensors (MOPITT, Tropospheric Emission Spectrometer - TES, and Atmospheric Infrared Sounder - AIRS) over most of the world (Warner *et al.*, 2013; Worden *et al.*, 2013). In particular, strong CO concentration decreases are seen from these satellite retrievals over East China and India (Worden *et al.*, 2013), where bottom-up inventories report increasing emissions (Granier *et al.*, 2011; Kurokawa *et al.*, 2013).

Atmospheric chemistry-transport models (ACTMs) prescribed with emission inventories are commonly used to analyze the role of emissions on the atmospheric concentration. Most of these simulations tend to underestimate CO concentrations in the mid to high latitudes of the northern hemisphere (NH), whereas they overestimate them over emission hotspots (Shindell *et al.*, 2006; Duncan *et al.*, 2007; Naik *et al.*, 2013; Stein *et al.*, 2014; Yoon and Pozzer, 2014). This bias reveals an incorrect balance between CO sources, at the surface and in the atmosphere, and CO sinks (Naik *et al.*, 2013). Understanding this model-data misfit is

challenging because surface emissions and chemical production each account for about half of the total CO sources, and because the sink term removes an amount of CO equivalent to all the sources within a few weeks. Changes in each source and sink term could have contributed to the observed CO concentration decrease, even though only CO emission trends are usually  
75 discussed (Khalil and Rasmussen, 1988; Novelli *et al.*, 2003; Duncan and Logan, 2008).

In principle, the attribution of the mean balance between sources and sinks and of their trends can be made with Bayesian inversion systems that infer the CO budget terms based on (i) measurements of CO and species related to the CO sources and sinks, (ii) some prior information about the budget terms and spatial distributions, (iii) a CTM model to link  
80 emissions and chemistry to concentrations, and (iv) a description of the uncertainty in each piece of information. Various inversion studies have estimated regional or global CO budgets using CO surface observations (Bergamaschi *et al.*, 2000; Pétron, 2002; Butler *et al.*, 2005) or satellites retrievals (Arellano *et al.*, 2004; Pétron *et al.*, 2004; Stavrakou and Müller, 2006; Chevallier *et al.*, 2009; Fortems-Cheiney *et al.*, 2009, 2011, 2012; Kopacz *et al.*, 2010;  
85 Hooghiemstra *et al.*, 2012a; Jiang *et al.*, 2013). Here, we use the inversion system Python Variational – Simplified Atmospheric Chemistry (PYVAR-SACS) of Pison *et al.* (2009), Chevallier *et al.* (2009) and Fortems-Cheiney *et al.* (2009, 2011, 2012) to infer the most likely origin of the observed CO concentration decrease over the past decade (2002-2011).

In contrast to most CO inversion systems cited above, which focused on a single species,  
90 PYVAR-SACS simultaneously assimilates observations of the main species in the chemical oxidation chain of CH<sub>4</sub>-CH<sub>2</sub>O-CO and methyl chloroform (MCF), a species that only reacts with OH and therefore informs about its concentration. The PYVAR-SACS system optimizes the interconnected sources and sinks of the four species in a statistically and physically consistent way at the model resolution of 3.75°×2.5° (longitude, latitude) on an 8-day basis,  
95 therefore being suitable for addressing the above-described attribution problem of the CO variations within the limit of the observation information content.

The primary data source about CO in this study is MOPITT, a multi-channel thermal infrared (TIR) and near infrared (NIR) instrument on board the EOS-Terra satellite (Deeter, 2003). MOPITT provides the longest consistent time series of satellite CO retrievals to date. The  
100 algorithm has undergone continuous improvements and the archive has been reprocessed

several times (Deeter *et al.*, 2013). Most of the above-cited satellite-based inversion studies used version 4 or earlier versions of the MOPITT CO retrievals, in which a noticeable instrumental drift was reported (Deeter *et al.*, 2010). In version 5, this drift has been corrected together with other improvements (Deeter *et al.*, 2013; Worden *et al.*, 2013). Here, we use the  
105 further improved version 6, that has no noticeable bias in the trends of the CO total column (Deeter *et al.*, 2014), to attribute the CO concentration decline by assimilation in our atmospheric inversion system.

The structure of the paper is as follows. Section 2 describes the inversion system and the datasets. Section 3 presents the inversion results on CO concentrations and associated trends.  
110 We show a brief evaluation of the inversion ability to fit the assimilated data and we cross evaluate the optimized surface CO concentrations against independent station measurements. Then, we compare the CO concentration trend in the MOPITT retrievals, in the surface measurements, and in corresponding modelling results before and after the inversion. Section 4 shows the trend analysis of the prior and the posterior simulated CH<sub>2</sub>O and OH  
115 concentrations. CH<sub>2</sub>O concentrations are representative of the chemical CO sources and we evaluate the model values against retrievals of its dry air column ( $X_{\text{CH}_2\text{O}}$ ) made from observations of Ozone Monitoring Instrument (OMI) aboard EOS Aura. OH regulates CO sinks, but is an extremely short-lived compound whose concentrations are difficult to measure (Mao *et al.*, 2012). Lacking direct global observation data, we discuss its  
120 uncertainties with two contrasting prior OH fields. Section 5 presents the inverted CO budget, including atmospheric burden, emission, chemical production and chemical loss. Section 6 summarizes this work, discusses the sources of uncertainties and provides some perspectives for future works.

## 125 **2 Method and data**

### **2.1 Inversion system**

The PYVAR Bayesian inversion system, initially introduced by Chevallier *et al.* (2005), aims at adjusting a series of target variables (jointly called  $\mathbf{x}$ ), so that they become consistent with both the atmospheric observations ( $\mathbf{y}$ ) and a priori state ( $\mathbf{x}^b$ ) given their respective

130 uncertainties, represented by error covariance matrices  $\mathbf{R}$  and  $\mathbf{B}$ . By iteratively minimizing the following cost function  $J$ , PYVAR finds the optimal solution for  $\mathbf{x}$  in a statistical sense:

$$J(\mathbf{x}) = \frac{1}{2}(\mathbf{x} - \mathbf{x}^b)^T \mathbf{B}^{-1}(\mathbf{x} - \mathbf{x}^b) + \frac{1}{2}(\mathbf{H}(\mathbf{x}) - \mathbf{y})^T \mathbf{R}^{-1}(\mathbf{H}(\mathbf{x}) - \mathbf{y})$$

where  $\mathbf{H}$  is the combination of a CTM and of an interpolation operator that includes the combination with the retrieval prior CO profiles and averaging kernels (AKs) for MOPITT.

135 Our CTM is the general circulation model of Laboratoire de Météorologie Dynamique (LMDz) version 4 (Hourdin *et al.*, 2006), nudged towards winds analysed by the European Centre for Medium-Range Weather Forecasts, run in an off-line mode with precomputed atmospheric mass fluxes, and coupled with the chemistry module SACS (Pison *et al.*, 2009). SACS is a simplification of the full chemistry model Interaction with Chemistry and Aerosols  
140 (INCA, Hauglustaine, 2004).

The chemical chain is shown in Fig. 1. It includes surface emissions of CO, CH<sub>4</sub>, CH<sub>2</sub>O and MCF. The 3D contribution of NMVOCs oxidation to CH<sub>2</sub>O production has been pre-calculated by the full chemistry transport model LMDz-INCA (Folberth *et al.*, 2006). OH links all the species together. Reaction kinetic and photolysis rates, as well as fields of  
145 species that are not represented as tracers in PYVAR-SACS (e.g. O<sub>1</sub>D, O<sub>2</sub>, Cl) are based on the LMDz-INCA simulation. The initial states are produced by LMDz-INCA. The CTM in PYVAR-SACS has a time step of 15 minutes for the dynamics (advection) and of 30 minutes for the physics (convection, boundary layer turbulence) and chemistry, a horizontal resolution of 3.75°×2.5° (longitude, latitude), and a vertical resolution of 19 eta-pressure levels from the  
150 surface to the top of the atmosphere.

The state vector  $\mathbf{x}$  contains the following variables as shown in the grey boxes in Fig. 1: (1) grid-point scaling factors for the initial mixing ratios of the four trace gas species (CO, CH<sub>4</sub>, CH<sub>2</sub>O, MCF); (2) grid-point 8-day mean surface emissions of CO, CH<sub>4</sub>, and MCF; (3) grid-point 8-day scaling factors to adjust the sum of CH<sub>2</sub>O surface emissions and CH<sub>2</sub>O  
155 production from NMVOC oxidation; (4) 8-day scaling factors to adjust the column-mean OH concentrations over 6 big boxes of the atmosphere over the globe: 3 latitudinal boxes (90°S-30°S, 30°S-0°, 0°-30°N) and 3 longitudinal boxes north of 30°N (North America:180°W-

45°W, Europe: 45°W-60°E, Asia: 60°E-180°E). The longitudinal division of the band north of 30°N is an improvement compared to previous PYVAR studies with 4 latitudinal bands in total to optimize OH. As there are available surface stations with long-term MCF observations within each of the sub-regions, thus allows adjusting separately continental differences of OH.

## 2.2 A priori information

Previous configurations of PYVAR-SACS have been described by [Chevallier \*et al.\* \(2009\)](#) and [Fortems-Cheiney \*et al.\* \(2011\)](#). We have improved the configuration as described below.

### 2.2.1 Prior sources and sinks

For prior anthropogenic fossil fuel and biofuel CO emissions, we use the monthly MACCity emission inventory of [Lamarque \*et al.\* \(2010\)](#) that arguably underestimates emissions less than other global inventories ([Granier \*et al.\*, 2011](#); [Stein \*et al.\* 2014](#)). For biomass burning, we updated the version of Global Fire Emissions (GFED) from version 2 ([van der Werf \*et al.\*, 2006](#)) to version 3.1 ([Van der Werf \*et al.\*, 2010](#)). The latter has various improvements including the definition of different fire types, with specific consideration for deforestation and peatland fires. We also increased the temporal resolution of biomass burning emissions from monthly to weekly (aggregated from GFEDv3.1 daily emissions, [Mu \*et al.\*, 2011](#)). Additionally, we consider in this study biochemical CO emissions from oceans, that were neglected before, based on an ocean biogeochemical model simulation ([Aumont and Bopp, 2006](#)). These monthly ocean CO fluxes add up to a global annual sum of 54 TgCO yr<sup>-1</sup> without inter-annual variability. We still consider neither biogenic CO emissions over land, nor surface CO deposition, because these two terms are relatively small and are of a similar order of magnitude ([Duncan \*et al.\*, 2007](#)). The prior CO emissions are summarised in Table 1 and the distribution of the mean annual prior CO surface emissions is shown in Fig. 2a. The relative contribution of biomass burning is shown in Fig. 2b.

The prior CH<sub>4</sub> and MCF emissions have also been updated compared to [Fortems-Cheiney \*et al.\* \(2012\)](#) and are similar to that of [Cressot \*et al.\*, \(2014\)](#). 3D HCHO production prior fields have been pre-calculated by LMDz-INCA ([Folberth \*et al.\*, 2006](#)), with prescribed NMVOC emission datasets detailed in [Fortems-Cheiney \*et al.\* \(2012\)](#). The prior distribution of mean

annual CO chemical sources in the troposphere from the oxidation of both CH<sub>4</sub> and NMVOCs are shown vertically integrated in Fig. 2c.

190 Previous PYVAR-SACS studies used prior OH information from a multi-year simulation by LMDz-INCA (Hauglustaine, 2004). Here, we use another field that was prepared for the international TransCom-CH<sub>4</sub> experiment of Patra *et al.*, (2011). The annual mean horizontal and vertical distribution of OH concentrations for both OH fields and their differences are shown in Fig. 3. Compared to the INCA-OH, the TransCom OH has a lower OH concentration in the NH, and a lower concentration over the Tropics and SH. Thus the  
195 TransCom-OH has a north-south inter-hemisphere ratio around 1, whereas the INCA-OH has a ratio of 1.2. There are also vertical differences between these two OH-fields: in general, TransCom-OH has higher OH concentrations in the mid-troposphere over the Tropics and in the top layers above 100 hPa, whereas INCA-OH has higher OH concentrations in the lower troposphere below 700 hPa. The prior distribution of the CO sinks simulated with TransCom-  
200 OH is shown vertically integrated in Fig. 2d.

### 2.2.2 Prior error statistics

The prior flux uncertainty, defined by the standard deviation (SD) of each grid-point 8-day flux, is described below. For CO emission uncertainties, we define the SD for each year based on the maximum value of the emission time series during the corresponding year for  
205 each grid point (noted as  $f_{\max}$ ), in order to account for the uncertainty of the fire timing. Then, to account for (i) the possibility of undetected small fires that can contribute to as much as 35% of the global biomass burning carbon emissions (Randerson *et al.*, 2012), and (ii) potentially higher CO emission factors during small fires that were not specifically considered in current fire emission inventories (van Leeuwen *et al.*, 2013), we define a fire  
210 emission threshold of  $1.0 \cdot 10^{-10}$  kg CO m<sup>-2</sup> s<sup>-1</sup>. If the prior emission is less than the threshold (no fire a priori, but there could be one in reality), the SD is set as 100% of  $f_{\max}$ ; otherwise (fire a priori, but possibly of a too small magnitude), the SD is set as the maximum value between  $1.0 \cdot 10^{-9}$  kg CO m<sup>-2</sup> s<sup>-1</sup> and 50% of  $f_{\max}$ . In such a way, we allow the system to relax the constraint on the prior emission to account for undetected small emissions, but we keep  
215 the global uncertainty ( $\sim 180$  TgCO yr<sup>-1</sup>) consistent with current bottom-up inventories

(Granier *et al.*, 2011; Van der Werf *et al.*, 2010). For simplicity, this error setting also serves for anthropogenic fuel consumption.

220 The prior CH<sub>4</sub> emission uncertainty is defined as 100% of the maximum value of the prior emissions in the grid cell and its eight neighbours in the corresponding month. The MCF prior emission uncertainty is set at ±10% of the flux, as its emissions are supposed to be well known. The uncertainty of CH<sub>2</sub>O production is assumed to be 100% of its concurrent prior CH<sub>2</sub>O production. The uncertainties of initial concentration scaling factors are set at 10% for the four species (CO, CH<sub>4</sub>, CH<sub>2</sub>O, MCF). Errors on OH 8-day scaling factors are set at ±10%.

225 The spatial error correlations of the a priori are assigned to all variables following Chevallier *et al.* (2007), defined by an e-folding length of 500 km over the land and 1000 km over the ocean. Temporal error correlations are defined by an e-folding length of 8 weeks for MCF and 2 weeks for the other species including OH. No inter-species flux error correlations are considered.

## 2.3 Observations for assimilation

### 230 2.3.1 Datasets

We assimilate three data streams: (i) MOPITTv6 satellite CO total column retrievals (noted as X<sub>CO</sub> hereafter) and surface in-situ measurements of (ii) CH<sub>4</sub> and (iii) MCF.

235 MOPITT retrievals are available since March 2000, but the instrument experienced a cooler failure from May 2001 to August 2001, which artificially changed the retrieval mean level (Deeter *et al.*, 2010). An instrument anomaly also led to a 2-month lack of data in 2009 from the end of July until September, without any significant change in the retrieval mean level. For the sake of consistency, given our focus on trends, we select the measurements for the decade from 2002 to 2011, during which both the MOPITT retrievals and the prior emission inventories are homogeneous (GFEDv3.1 has not been publicly updated for the years after 240 2011).

We use the level 2 “multispectral” near and thermal infrared (NIR/TIR) CO retrievals of MOPITTv6 that offer the best description of CO in the lower troposphere among the MOPITT products (Deeter *et al.*, 2014). The MOPITT vertical profiles (prior and retrieved

CO profiles and associated AKs) are defined on ten vertical pressure levels. Given the limited  
245 vertical resolution of the retrievals and the focus on surface emissions, it has been common  
practice in previous inversion studies starting from Pétron *et al.* (2004) to assimilate the 700-  
hPa pressure level retrievals only, as a good compromise between proximity to the surface  
and limited noise. However, Deeter *et al.* (2014) noted that the retrievals at some individual  
250 vertical levels still suffered from small bias drifts while such drifts were not seen in the  
retrieved integrated columns. Furthermore, the interpretation of vertically-integrated columns  
in the inversion is less hampered by flaws in CTM vertical mixing and vertical sink  
distribution than for level retrievals (Rayner and O'Brien, 2001). For these two reasons, we  
assimilate the column retrievals rather than level retrievals. Night-time observations,  
observations with solar zenith angle larger than 70 degrees, with latitudes within 25 degrees  
255 from the poles, or with surface pressures less than 900 hPa are excluded, since they may be of  
lower quality or more difficult to model (Fortems-Cheiney *et al.*, 2011). We average the  
 $22 \times 22$  km<sup>2</sup> retrievals at the  $3.75^\circ \times 2.5^\circ$  model resolution within 30-minute time steps. The  
model X<sub>CO</sub> retrievals are calculated in a consistent way as in the MOPITT X<sub>CO</sub> retrievals with  
their original prior CO profiles and AKs averaged for each model grid.

260 Surface measurements of CH<sub>4</sub> and MCF from various networks are assimilated together with  
MOPITT X<sub>CO</sub>. The datasets are downloaded from the World Data Centre for Greenhouse  
Gases (WDCGG, <http://ds.data.jma.go.jp/gmd/wdcgg/>). Stations that recorded more than 6  
years of data without gaps larger than 1 year are included. The list of stations is given in  
Tables S1 and S2. For the surface measurements, a data filtering process is conducted in  
265 order to remove outliers that the global model may not be able to capture. We exclude (i)  
observations exceeding  $3\sigma$  of the de-trended and de-seasonalized daily time series and (ii)  
observations whose misfit against the prior simulation exceeds  $3\sigma$  of the de-trended and de-  
seasonalized misfit between observations and forward modelling values.

### 2.3.2 Observation error statistics

270 The observation error covariance matrix  $\mathbf{R}$  is diagonal in order to simplify calculations.  
Observation errors are combinations of measurement errors (quantified by the data  
providers), representativeness errors and CTM errors. For X<sub>CO</sub>, as we have averaged a large  
amount of observations in each grid-box (see Section 2.3.1), the representativeness error is

effectively much reduced and is not considered specifically. The CTM error is set at 30%  
275 (SD) of the modelled values for X<sub>CO</sub>. For CH<sub>4</sub> and MCF, synoptic variability (estimated from  
the residues of de-trended and de-seasonalized data) is used as a proxy for the CTM and  
representativeness errors, which largely dominate the observation error. The global mean  
measurement error for X<sub>CO</sub> is around 6.4±2.9 ppb, which is approximately 8.2±1.9 % of  
280 corresponding X<sub>CO</sub> observations. The measurement errors are set as 3 ppb for CH<sub>4</sub> and 1.2  
ppt for MCF if not explicitly provided by the surface observation datasets.

## 2.4 Observations for cross evaluation

We use two datasets for independent evaluation of the inversion results.

The first one is made of CO surface observations archived at the WDCGG. The same site  
selection and data filtering process as for CH<sub>4</sub> and MCF surface measurements are applied  
285 (see the list of stations in Table S3).

The second evaluation dataset gathers CH<sub>2</sub>O total columns retrieved from OMI by the  
Smithsonian Astrophysical Observatory (SAO). We use version 3, release 2, of this product  
([González Abad \*et al.\*, 2015](#)). Since this data is not available before mid-2004, it does not  
cover our study period completely: for the sake of consistency, we do not assimilate it (in  
290 contrast to [Fortems-Cheiney \*et al.\*, 2012](#)) and we keep it for evaluation. We select  
observations that are tagged as “good” by the provider’s quality flag, which have a solar  
zenith angle less than 70 degrees, a cloud cover below 20%, and are not affected by the “row  
anomaly”.

## 2.5 Trend analysis

295 The long-term trend in this study is estimated by least-square curve fitting of the following  
function, which includes a constant, a linear component, and seasonal variations represented  
by four harmonics:

$$f(t) = a_0 + a_1 t + \sum_{n=1}^4 c_n [\sin(2n\pi t + \varphi_n)]$$

If not particularly specified, all the trends mentioned in this paper refer to  $a_1$ .

### 3 CO concentrations and associated trends

#### 3.1 Evaluation of the inversion framework's ability to fit the data

Fig. 4a shows the time series of global mean mole fraction of the MOPITT  $X_{CO}$  retrievals (black), the prior (blue) and the posterior (red)  $X_{CO}$  retrievals (calculated from model simulations with the MOPITT prior profiles and averaging kernels). Compared to the MOPITT  $X_{CO}$ , the prior  $X_{CO}$  simulation is on average 15% lower when modelled with TransCom-OH and 17% lower when modelled with INCA-OH. The global mean posterior  $X_{CO}$  fits the observation irrespective of the OH field used.

The spatial distribution of the multiyear mean  $X_{CO}$  observed by MOPITT (2002-2011) shows a latitudinal gradient from north to south, with some high values over East Asia, Africa and central South America (Fig. 4b). The regional mean bias of  $X_{CO}$  in the prior and the posterior modelling compared to the MOPITT data are summarized in Table 2. The prior simulation is generally lower than the observations except in parts of Indonesia and India (Fig. 4c). This negative bias agrees with previous studies (Arellano *et al.*, 2004; Fortems-Cheiney *et al.*, 2011; Hooghiemstra *et al.*, 2012a, Naik *et al.*, 2013; Shindell *et al.*, 2006), and thus calls attention to understanding and correcting it appropriately (Stein *et al.*, 2014). The optimized CO concentrations fit the measurements quite well (Fig. 4d), illustrating the inversion's ability to fit the data.

Similarly for  $CH_4$  and MCF, Table 3 summarizes the mean biases and residual root mean squares (RMS) of the prior and posterior modelling values compared to the station observations that are assimilated in the system over four latitudinal bands. The inversion fits the assimilated data fairly well, with a considerable decrease in both the mean biases and the RMS (Table 3).

The mean biases of the prior and posterior simulations compared to independent surface in-situ CO measurements are also summarized for each region in Table 2. For the oceanic background stations (over 27 model grid cells), the magnitude of the model-data misfits decreased considerably after inversion. Over land, the changes in model-data misfit after inversion are more heterogeneous. The prior bias is in general negative, whereas the sign

330 changed from negative to positive for the posterior. The magnitude of the posterior bias (also the RMS, not shown in the table) decreased significantly in West Europe (WSEU), South East Asia (SEAS) and North Hemisphere Africa (NHAF), and they are of similar magnitudes in Boreal North America (BONA) and the USA. However, the mean bias and RMSs increased in South Hemisphere Africa (SHAF) and Australia (AUST).

335 This seemingly deterioration of the modelled surface concentrations could be explained by several reasons: First, surface station measurements and model grids (2.5x3.75 degree) have different spatial representativeness. In fact, at most background oceanic stations, the model-data misfit suggests an overall improvement after inversion. Second, the vertical sensitivities are different between satellite column retrievals and surface observations (Hooghiemstra *et al.*, 2012). Over regions where fire emission injection heights are sometimes above the 340 boundary layer (Cammass *et al.*, 2009) or where chemical CO sources in the mid-troposphere contributes significantly to the CO column (Fisher *et al.*, 2015), the surface CO concentrations are less influenced by these sources, but the model may not capture this vertical distribution of sources. Third, there might be a model bias in modelling the vertical CO profiles in the CTM (Jiang *et al.*, 2013), for instance, when the vertical mixing in the 345 model is too conservative, it could lead to a positive bias at the surface, because the sources are adjusted to fit the satellite data. Nevertheless, such discrepancies between  $X_{CO}$  column and surface concentration do not seem to bear a significant trend. For instance, significant trends in the prior misfits were found in the NH ( $0.67 \pm 0.24$  ppb yr<sup>-1</sup>), NH-Tropics ( $0.77 \pm 0.16$  ppb yr<sup>-1</sup>) and SH-Tropics ( $-0.42 \pm 0.14$  ppb yr<sup>-1</sup>), and they are corrected in the posterior misfits 350 to non-significant after assimilation.

### 3.2 Distribution of trends in CO concentrations

The spatial distributions of trends in the MOPITT  $X_{CO}$  and in the prior and the posterior  $X_{CO}$  over the period from 2002 to 2011 are shown successively in Fig. 5. Regional mean trends in both the  $X_{CO}$  and surface CO concentrations are summarized in Table 2.

355 MOPITT  $X_{CO}$  retrievals show negative trends in most regions of the world except for the Sahel region in Africa and some areas of central South America and India (Fig. 5a). In the MOPITT retrievals, the negative trends are particularly large over Indonesia ( $-1.20$  ppb yr<sup>-1</sup>), South East Asia ( $-1.23$  ppb yr<sup>-1</sup>) and the Northern Pacific and Atlantic Ocean ( $-1.15$  ppb yr<sup>-1</sup>).

The global average trend in the MOPITT  $X_{CO}$  is  $-0.67 \text{ ppb yr}^{-1}$ , accounting for a decrease of  
360 around  $0.91\% \text{ yr}^{-1}$  over the globe, and the trends in the prior and posterior  $X_{CO}$  retrievals are  $-0.12 \text{ ppb yr}^{-1}$  ( $-0.28\% \text{ yr}^{-1}$ ) and  $-0.70 \text{ ppb yr}^{-1}$  ( $-0.93\% \text{ yr}^{-1}$ ) respectively. The spatial correlations between the trends of the MOPITT  $X_{CO}$  and the prior/posterior  $X_{CO}$  are 0.55 and 0.81 respectively, showing considerable improvements after inversion.

In general, negative trends in the prior  $X_{CO}$  are underestimated (Fig. 5b and Table 2), and  
365 positive trends are simulated over Southeast Asia (19%), South Hemisphere South America (41%), South Africa (27%), Australia (28%), with percentages of model grid cells that have significant positive trends noted in the brackets. In addition, 22% of the oceanic grid cells are modelled with positive trends in the prior simulation, but none is noticed in the MOPITT column retrievals (Deeter *et al.*, 2014). Trends in the posterior  $X_{CO}$  generally agree with the  
370 MOPITT  $X_{CO}$  and the positive trends in the prior  $X_{CO}$  are corrected (Fig. 5c and Table 2).

Surface in-situ measurements also show a general negative trend in CO concentration (Table 2). The negative trends from in-situ CO stations have the largest magnitude in the NH mid-latitudes over West Europe ( $-2.7 \pm 1.7 \text{ ppb yr}^{-1}$ ) and the USA ( $-1.6 \pm 0.9 \text{ ppb yr}^{-1}$ ). Smaller trends are found in the SH in-situ sites ( $-0.32 \pm 0.14 \text{ ppb yr}^{-1}$ ). The trends over Asia indicate  
375 large spatial heterogeneity ( $-1.6 \pm 1.3 \text{ ppb yr}^{-1}$ ) and the trends over the Tropics show a small but insignificant increase ( $0.3 \pm 1.6 \text{ ppb yr}^{-1}$ ), but these regions are represented by a limited number of stations.

Compared to these surface in-situ measurements, the prior simulation generally tends to underestimate the magnitude of the negative ones, and the posterior slightly overestimate  
380 them. The global mean trends are  $-1.3 \text{ ppb yr}^{-1}$  ( $-1.1\% \text{ yr}^{-1}$ ) in the observation,  $-0.87 \text{ ppb yr}^{-1}$  ( $-0.75\% \text{ yr}^{-1}$ ) in the prior simulations, and  $-1.9 \text{ ppb yr}^{-1}$  ( $-1.2\% \text{ yr}^{-1}$ ) in the posterior simulations. However, it is noted that the global mean trends are only represented by 72 stations that are not evenly distributed over the globe. Positive trends in the prior simulated surface CO are less visible compared to the total column as shown in Fig 5b and Table 2. It  
385 could be explained by the respective vertical weighting of these two observation types, but the difference may also be enhanced by changes in the MOPITT AKs if the retrieval prior is biased (Yoon *et al.*, 2013). However, this comparison is limited by the representativeness of a few sites.

## 390 4 Concentrations of CH<sub>2</sub>O and OH

### 4.1 CH<sub>2</sub>O columns

The mean time series of CH<sub>2</sub>O total columns for four latitudinal zones are shown in Fig. 6. X<sub>CH<sub>2</sub>O</sub> retrievals were not assimilated (contrary to the CH<sub>4</sub> and MCF surface measurements that affect the sources and sinks of CH<sub>2</sub>O in the inversion), and the inversion actually does  
395 not change X<sub>CH<sub>2</sub>O</sub> much. This suggests that the differences between simulated and satellite-retrieved X<sub>CH<sub>2</sub>O</sub> are mainly caused by the prior NMVOC emissions used in the full chemistry run of LMDz-INCA. The latitudinal mean values of prior/posterior modelled X<sub>CH<sub>2</sub>O</sub> agree fairly well with the OMI retrievals without any obvious bias, but the seasonal cycle is different especially in the Northern mid-high latitudes both in phase and in amplitude (Fig.  
400 6a). The OMI X<sub>CH<sub>2</sub>O</sub> retrievals, the prior and the posterior simulations all agree about the absence of a significant trend in the latitudinal average of X<sub>CH<sub>2</sub>O</sub> for the period from 2005 to 2011, which is consistent with the hypothesis that the equilibrium between the oxidation of hydrocarbons into CH<sub>2</sub>O and the sink of CH<sub>2</sub>O into CO has not significantly changed, at least at continental scales. We note that the OMI X<sub>CH<sub>2</sub>O</sub> retrievals describe some trends at smaller  
405 scales, like positive trends of  $3\pm 0.8\%$  yr<sup>-1</sup> over East Asia (De Smedt *et al.*, 2010) and negative trends of  $-1.9\pm 0.6\%$  yr<sup>-1</sup> over the Amazon, but they are not significant for the mean values of large latitudinal bands and are thus considered not large enough to influence the global CO budget.

### 4.2 OH concentrations

410 Fig. 7 shows the latitudinal average of the prior (blue) and posterior (red) OH concentrations for the 6 big regions over which OH is optimized (see Section 2.1). This figure reports the two inversions that use either TransCom-OH (solid lines) or INCA-OH (dashed lines; see Section 2.2.1). INCA has higher OH concentrations than TransCom in the NH in particular during summer, but lower OH concentrations in the SH Tropics all year long and slightly  
415 lower concentrations in the SH mid-high latitudes (South of 30S) during summer peaks.

In general, larger corrections are applied by the inversion to INCA-OH than to TransCom-OH. The inversion system adjusts the INCA-OH concentrations towards TransCom-OH by

downscaling the OH concentrations in the NH during summers, especially over Asia, where INCA-OH is considerably higher than the TransCom-OH (Fig. 3). A small reduction of the TransCom-OH concentrations is also seen in the SH.

The two inversions do not produce significant trends in OH during the study period for most regions, except for a very small positive trend in the SH Tropics (+0.2% yr<sup>-1</sup> with TransCom-OH and +0.7% yr<sup>-1</sup> with INCA-OH) and a small negative trend in the SH mid-high latitudes (-0.4% yr<sup>-1</sup> in TransCom-OH and -0.3% yr<sup>-1</sup> in INCA-OH). Such small and insignificant trends are considered to be of minor importance for the CO trends. The OH scaling is addressed more in details in section 5.1 when discussing CO sinks.

## 5 Optimized sources and sinks of CO

After having documented the prior and the posterior misfits with MOPITTv6 and with cross validation data for the latitudinal mean values and for the trends, which lends support to the consistency of the inversion results with these data-streams, we now turn to the implications for CO sources and sinks.

### 5.1 Inverted CO budget

The global annual CO atmospheric burden, surface emissions, chemical production, and chemical loss of the prior and the posteriors with the two OH experiments from 2002 to 2011 are shown in Fig. 8. Averaging over the 10 years, a considerable increase of the mean CO atmospheric burden (+23%, in dark green) is seen in the posterior compared to the prior simulation. Accordingly, increases of CO emissions (+50%, in red) and chemical sinks with OH (+23%, in purple) are produced in the posterior, whereas only a very small change is noticed for the CO chemical sources (+1%, in blue). The magnitude of the increment in the global CO emissions is larger compared to previous studies that assimilate the 700 hPa retrieval levels of MOPITT using a similar inversion set up (Fortems-Cheiney *et al.*, 2011, 2012). The cross evaluation against surface station measurements also shows a considerable positive bias in the posterior CO concentration (section 3.1), which implies a potential bias in the modelling of vertical CO profiles. Nevertheless, for our study here focusing on trends, such systematic model error do not seem to harm the robustness of the trends as shown in

section 3 and 4. The chemical sink of CO is a function of both CO and OH. Given the results for OH adjustments shown in section 4.2 (generally small reduction from the prior OH), the increase of the CO sink in the posterior is thus mainly due to the increase of CO concentrations after assimilation.

The inversion produces a negative trend of around 10% per decade in the global atmospheric burden of CO ( $-5.1 \pm 0.9 \text{ TgCO yr}^{-1}$  with TransCom-OH and  $-4.6 \pm 0.8 \text{ TgCO yr}^{-1}$  with INCA-OH), which is twice the negative trend of CO atmospheric burden produced by the prior emissions ( $-1.6 \pm 0.6 \text{ TgCO yr}^{-1}$ , i.e. a decrease of 5% per decade in the simulated CO burden).

For CO sources, the trend of prior CO emissions is of  $-11.1 \pm 4.4 \text{ TgCO yr}^{-1}$  (equivalent to a decrease of 10% per decade). This is mostly contributed by the negative trend in biomass burning emissions in GFEDv3.1 ( $-10.6 \pm 3.7 \text{ TgCO yr}^{-1}$ ) and by a very small decrease in anthropogenic emissions in MACCity ( $-0.68 \pm 0.4 \text{ TgCO yr}^{-1}$ ) from 2002 to 2011. Compared to the prior emissions, a two-fold steeper negative trend in terms of percentages is found in the posterior CO emissions, 24% per decade with TransCom-OH ( $-40 \pm 7.2 \text{ TgCO yr}^{-1}$ ) and 22% per decade with INCA-OH ( $-37 \pm 7.1 \text{ TgCO yr}^{-1}$ ). A small positive trend ( $2.8 \pm 7.1 \text{ TgCO yr}^{-1}$ , equivalent to an increase of 2% per decade) is produced in the prior CO chemical production, mostly contributed by the increase of methane oxidation. The posterior CO chemical production shows a small negative trend. Yet, as  $\text{CH}_2\text{O}$  concentrations are not constrained by observations, this small trend may result from the system's inability to differentiate the two CO sources between surface emissions and chemical oxidations.

For the CO sink, a larger trend in the posterior ( $-46.3 \pm 8.3 \text{ TgCO yr}^{-1}$ , 16% per decade with TransCom-OH and  $-39.3 \pm 8.0 \text{ TgCO yr}^{-1}$ , 13% per decade with INCA-OH) is found, while there is no significant trend in the prior chemical sink. This negative trend in the posterior is mostly due to the decrease of CO concentrations in the atmosphere that change the amount of CO oxidized by OH, and only very small trends in the OH concentrations are found by the inversion. Such small trends are considered of very small effect on the CO trends. The OH concentrations are optimized for 6 big regions over the globe and the MCF concentrations are monitored at background sites only, which allows a coarse zonal estimate of OH but leaves spatially heterogeneous land areas unconstrained, e.g. polluted areas near cities (Hofzumahaus *et al.*, 2009), forests with high NMVOC emissions (Lelieveld *et al.*, 2008) or

biomass burning plumes (Folkens *et al.*, 1997; Rohrer *et al.*, 2014). Therefore, sub-regional trends in OH, if they exist, are not necessarily captured in this study. In addition, with the exponential decrease of MCF concentrations in recent years (only a few parts per trillion, ppt, at the current level), the constraining strength of MCF on OH in the inversion system may not be even from 2002 to 2011, even though the same sites and a similar number of observations were assimilated. Nevertheless, the zonal trend of OH should still be constrained throughout most of the period and previous studies suggest that the inter-annual change of global OH concentration is within 5% (Montzka *et al.*, 2011).

## 485 **5.2 Regional distribution of trends in CO emissions**

The distributions of trends in CO emissions after optimization are very consistent using either TransCom-OH or INCA-OH (Fig. 9); therefore, only trends of TransCom-OH experiments are discussed here. The relative contribution of biomass burning to the total land surface emissions estimated in the prior emission is shown in Fig. 2b. The time series of the prior and the two posterior annual CO emissions using two different OH fields are shown for each sub-region in Fig. 10. The division in sub-regions is illustrated in Fig. A1. As shown in Fig. 10, the choice of prior OH concentrations could potentially have a large impact on the regional CO emission estimates; nevertheless, the inverted emission trends are quite robust and we do not discuss further in this paper the regional emission increments and the sensitivities of inverted fluxes to prior OH or chemical CO productions.

For the boreal regions where CO emissions are mainly due to biomass burning (Boreal Asia - BOAS and Boreal North America - BONA), the same sign of the trends in CO emissions is mostly kept between the prior and the posterior, but the amplitude of the trends are updated into larger values, as are the emission amounts. It should be noted that MOPITT CO retrievals over high latitudes beyond 65° are not included in the assimilation.

For the NH mid-latitudes where CO emissions are mainly due to fossil fuel and biofuel burning emissions (USA, West Europe - WSEU, East Europe - ESEU, Middle East - MIDE, South Central Asia - SCAS, South East Asia - SEAS), consistencies between the trends in the prior and the posterior CO emissions are found in the developed countries (Fig. 9). For example in the USA and WSEU regions, decreasing trends produced by the emission inventories generally agree with the atmospheric signals (Lamarque *et al.*, 2010). On the

contrary, the inversion changes the sign of the CO trend over SEAS (including China) and SCAS (including India), where the prior emissions suggested a significant increase. Consistent with our posterior emissions, a gradual decrease of CO emissions in China after the year 2005 was actually deduced from CH<sub>4</sub>/CO<sub>2</sub> and CO/CO<sub>2</sub> correlations observed off the coast of East Asia from 1999-2010 (Tohjima *et al.*, 2014). A decrease of the emission factors of other co-emitted species of CO during fossil fuel or biofuel combustion has also been noted: for instance, a decrease of black carbon emission factors in China and India was reported by Wang *et al.* (2014), and a decrease in the relative ratio of NO<sub>x</sub> to CO<sub>2</sub> from 2003 to 2011 was observed from satellite retrievals over East Asia (Reuter *et al.*, 2014). These studies and our results suggest that combustion technology improvements in East Asia resulted in emission factor reduction to an extent that outweighs the impact of increasing fossil fuel burning. In this scenario, emission inventories would well report the latter but not the former that is more difficult to quantify. In addition, trends of fossil fuel emissions are updated (Lamarque *et al.*, 2010) but not trends of biofuel burning, especially for traditional biofuels (Yevich and Logan, 2003). A small difference in the trend of CO emissions in East Europe (ESEU) is also noticed (not significant though), an emission peak in the year 2010 is inferred from the inversion.

For the tropical and sub-tropical regions, where CO emissions are mainly attributed to biomass burning, the inversion does not change the sign of trends over Indonesia (INDO). The positive trends of the prior emissions over the Indo-China Peninsula (2% yr<sup>-1</sup>) are updated into negative ones (-5.6% yr<sup>-1</sup>) by the inversion. Negative trends over Australia except for the central area (on average -5.3% yr<sup>-1</sup>), and over SHSA (-3% yr<sup>-1</sup>, but not significant for the regional mean) are largely enhanced compared to the prior trends (Fig. 9). The spatial distribution of this negative trend is consistent with the new version of GFEDv4 burned area (not used in this study) (Giglio *et al.*, 2013), which accounts for small fires that were not explicitly included in GFEDv3.1 used here as the prior. In Australia, the decrease of CO emissions might be explained by decreased fire emissions (Poulter *et al.*, 2014). The decrease in SHSA could be attributed to a decrease of deforestation fires in recent years, especially after 2005 (Meyfroidt and Lambin, 2011), although there are uncertainties in the overall deforestation rates (Kim *et al.*, 2015).

The change in trends between the prior and the posterior CO emissions is more heterogeneous over Africa (Northern Hemisphere Africa - NHAF and Southern Hemisphere Africa - SHAF). Decreases in the burned area have been observed over the NHAF Sahel region, as are decreases in the prior CO emissions, which are explained by changes in both precipitation and the conversion of savannah into cropland (Andela and van der Werf, 2014). But positive trends in CO emissions are inferred by the atmospheric inversion especially since 2006, except for some small areas. The different signs of the trend in burned area (or the prior CO emissions) and the posterior CO emissions may be explained by the change in CO emission factors that could vary a lot with the conversion of fire type from savannah fire to agricultural burning and also with precipitation change (van Leeuwen *et al.*, 2013). In addition, increases of anthropogenic fossil fuel and biofuel emission in the NHAF region could also contribute to some of the differences (Al-mulali and Binti Che Sab, 2012). Differences between the prior and the posterior CO emissions are also noticed for the central part of the SHAF. The increase in the GFED4 burned area is explained by the increase of precipitation that allows more fuel accumulation, as driven by the El Niño/Southern Oscillation (ENSO) changes from El Niño to La Niña dominance over the recent decade (Andela and van der Werf, 2014). The opposite negative trend of CO emissions in the posterior could be explained by a decrease in CO emission factors when the fuel load and combustion completeness are high so that less carbon is emitted in the form of CO; but the dynamics of emission factors are not modelled in the bottom-up estimation (van Leeuwen *et al.*, 2013). In addition, small fires that are not considered in our prior biomass emissions could also contribute to such differences (Randerson *et al.*, 2012).

## 560 **6 Conclusion**

CO concentrations observed by both MOPITTv6 satellite  $X_{CO}$  retrievals and surface in-situ measurements show significant negative trends over most of the world from 2002 to 2011. The CO concentration trends in the forward CTM simulations prescribed with CO emission inventories show considerable inconsistency with the observed MOPITT  $X_{CO}$  from 2002 to 2011. By assimilating MOPITTv6  $X_{CO}$  and surface measurements of  $CH_4$  and MCF, the inversion system suggests that the decrease in the atmospheric CO concentrations is mainly

attributable to a decrease of 23% in surface emissions during the study period at the global scale. The trends in the prior and the posterior CO emissions agree well with each other over the USA and Western Europe. The largest differences between the prior and the posterior CO  
570 emission trends are noticed for South East Asia, Australia and parts of South America and Africa. Decreases of CO emissions are found in Central China, while the prior emission inventories suggest increases. This emission decrease is probably caused by a large decrease of emission factors due to technology improvements that outweigh the increase of emission activities. CO emissions from biomass burning decreased considerably in Indonesia and  
575 Australia. For Africa, the contrasts of trends between the prior and the posterior likely reflect different trends between satellite-detected burned area and CO emissions due to changes in combustion completeness, CO emission factors, and the relative contribution of small fires. The amplitude of the trends also differs in many other regions, illustrating the original information brought by atmospheric inversions about CO emissions.

580 No significant trend is found in the latitudinal-mean OH concentrations, and a sensitivity test made with two different OH fields suggests consistent results in the OH trend. It is however noted that we optimized OH over six big-regions globally, and sub-regional trends in the OH concentrations, if they exist, are not accounted for in this study. We also acknowledge the limited information content of MCF to constrain OH in recent years over the study period.  
585 For chemical CH<sub>2</sub>O production from NMVOC oxidation, the system has the potential to generate regional increments, but CH<sub>2</sub>O is not assimilated here due to limited temporal coverage of the OMI data from 2005 to 2011. Assimilating observations of CH<sub>2</sub>O and other chemically connected species could inform more about regional CO budgets, in particular the chemical sources and sinks, and therefore could further improve the top-down estimation of  
590 CO budgets for each region in future studies.

## Acknowledgements

595 The authors acknowledge the support of the French Agence Nationale de la Recherche (ANR)  
under grant ANR-10-BLAN-0611 (project TropFire). F.C. is funded by the European  
Commission under the EU H2020 Programme (grant agreement No. 630080, MACC III). The  
NCAR MOPITT and the SAO OMI retrievals are available from  
<https://www2.acd.ucar.edu/mopitt> and <http://disc.sci.gsfc.nasa.gov/Aura/data->  
600 [holdings/OMI/omhcho\\_v003.shtml](http://disc.sci.gsfc.nasa.gov/Aura/data-holdings/OMI/omhcho_v003.shtml), respectively. We thank both institutes for having brought  
this data into open access and thank Dr. González Abad for helpful information about the  
OMI product. Similarly, we also acknowledge the WDCGG for providing the archives of  
surface station observations for MCF, CH<sub>4</sub> and CO. We thank the following persons who have  
participated to the surface in-situ measurements through various networks: NOAA (E.  
605 Dlugokencky, G.S. Dutton, J.W. Elkins, S.A. Montzka, P.C. Novelli), CSIRO (P.B.  
Krummel, R.L. Langenfelds, L.P. Steele), EC (D. Worthy), Empa (B. Buchmann, M.  
Steinbacher, L. Emmenegger), JMA (Y. Fukuyama), LSCE (M. Ramonet), NIWA (G.  
Brailsford, S. Nichol, R. Spoor), UBA (K. Uhse), UNIURB (J. Arduini), and AGAGE (P.J.  
Fraser, C.M. Harth, P.B. Krummel, S. O'Doherty, R. Prinn, S. Reimann, L.P. Steele, M.  
610 Vollmer, R. Wang, R. Weiss, D. Young). Finally, we wish to thank F. Marabelle and his team  
for computer support at LSCE.

## References

- 615 Al-mulali, U. and Binti Che Sab, C. N.: The impact of energy consumption and CO<sub>2</sub> emission on the economic growth and financial development in the Sub Saharan African countries, *Energy*, 39(1), 180–186, doi:10.1016/j.energy.2012.01.032, 2012.
- Angelbratt, J., Mellqvist, J., Simpson, D., Jonson, J. E., Blumenstock, T., Borsdorff, T., Duchatelet, P., Forster, F., Hase, F., Mahieu, E., De Mazière, M., Notholt, J., Petersen, A. K.,  
620 Raffalski, U., Servais, C., Sussmann, R., Warneke, T. and Vigouroux, C.: Carbon monoxide (CO) and ethane (C<sub>2</sub>H<sub>6</sub>) trends from ground-based solar FTIR measurements at six European stations, comparison and sensitivity analysis with the EMEP model, *Atmos. Chem. Phys.*, 11(17), 9253–9269, doi:10.5194/acp-11-9253-2011, 2011.
- Arellano, A. F., Kasibhatla, P. S., Giglio, L., van der Werf, G. R. and Randerson, J. T.: Top-  
625 down estimates of global CO sources using MOPITT measurements, *Geophys. Res. Lett.*, 31(1), L01104, doi:10.1029/2003GL018609, 2004.
- Aumont, O. and Bopp, L.: Globalizing results from ocean in situ iron fertilization studies, *Global Biogeochem. Cycles*, 20(2), GB2017, doi:10.1029/2005GB002591, 2006.
- Belattaf, A.: Modélisation des sources océaniques de CO et d'isoprène, Master Thesis U.  
630 Versailles Saint-Quentin, 32pp, 2012.
- Bergamaschi, P., Hein, R., Heimann, M. and Crutzen, P. J.: Inverse modeling of the global CO cycle: 1. Inversion of CO mixing ratios, *J. Geophys. Res.*, 105(D2), 1909, doi:10.1029/1999JD900818, 2000.
- Butler, T. M., Rayner, P. J., Simmonds, I. and Lawrence, M. G.: Simultaneous mass balance  
635 inverse modeling of methane and carbon monoxide, *J. Geophys. Res.*, 110(D21), D21310, doi:10.1029/2005JD006071, 2005.
- Cammas, J.-P., Brioude, J., Chaboureau, J.-P., Duron, J., Mari, C., Mascart, P., Nédélec, P., Smit, H., Pätz, H.-W., Volz-Thomas, A., Stohl, A. and Fromm, M.: Injection in the lower stratosphere of biomass fire emissions followed by long-range transport: a MOZAIC case  
640 study, *Atmos. Chem. Phys.*, 9(15), 5829–5846, doi:10.5194/acp-9-5829-2009, 2009.
- Chevallier, F., Bréon, F.-M. and Rayner, P. J.: Contribution of the Orbiting Carbon Observatory to the estimation of CO<sub>2</sub> sources and sinks: Theoretical study in a variational data assimilation framework, *J. Geophys. Res.*, 112(D9), D09307, doi:10.1029/2006JD007375, 2007.
- 645 Chevallier, F., Fisher, M., Peylin, P., Serrar, S., Bousquet, P., Bréon, F. M., Chédin, A. and Ciais, P.: Inferring CO<sub>2</sub> sources and sinks from satellite observations: Method and application

to TOVS data, *J. Geophys. Res.*, 110(D24), 2005.

650 Chevallier, F., Fortems, A., Bousquet, P., Pison, I., Szopa, S., Devaux, M. and Hauglustaine, D. A.: African CO emissions between years 2000 and 2006 as estimated from MOPITT observations, *Biogeosciences*, 6(1), 103–111, 2009.

655 Cressot, C., Chevallier, F., Bousquet, P., Crevoisier, C., Dlugokencky, E. J., Fortems-Cheiney, A., Frankenberg, C., Parker, R., Pison, I., Scheepmaker, R. A., Montzka, S. A., Krummel, P. B., Steele, L. P. and Langenfelds, R. L.: On the consistency between global and regional methane emissions inferred from SCIAMACHY, TANSO-FTS, IASI and surface measurements, *Atmos. Chem. Phys.*, 14(2), 577–592, doi:10.5194/acp-14-577-2014, 2014.

Deeter, M. N.: Operational carbon monoxide retrieval algorithm and selected results for the MOPITT instrument, *J. Geophys. Res.*, 108(D14), 4399, doi:10.1029/2002JD003186, 2003.

660 Deeter, M. N., Edwards, D. P., Gille, J. C., Emmons, L. K., Francis, G., Ho, S. P., Mao, D., Masters, D., Worden, H., Drummond, J. R. and Novelli, P. C.: The MOPITT version 4 CO product: Algorithm enhancements, validation, and long-term stability, *J. Geophys. Res.*, 115(D7), doi:DOI: 10.1029/2009JD013005, 2010.

665 Deeter, M. N., Martínez-Alonso, S., Edwards, D. P., Emmons, L. K., Gille, J. C., Worden, H. M., Pittman, J. V., Daube, B. C. and Wofsy, S. C.: Validation of MOPITT Version 5 thermal-infrared, near-infrared, and multispectral carbon monoxide profile retrievals for 2000–2011, *J. Geophys. Res. Atmos.*, 118(12), 6710–6725, 2013.

Deeter, M. N., Martínez-Alonso, S., Edwards, D. P., Emmons, L. K., Gille, J. C., Worden, H. M., Sweeney, C., Pittman, J. V., Daube, B. C. and Wofsy, S. C.: The MOPITT Version 6 product: algorithm enhancements and validation, *Atmos. Meas. Tech. Discuss.*, 7(6), 6113–6139, doi:10.5194/amtd-7-6113-2014, 2014.

670 Duncan, B. N. and Logan, J. A.: Model analysis of the factors regulating the trends and variability of carbon monoxide between 1988 and 1997, *Atmos. Chem. Phys.*, 8(24), 7389–7403, doi:10.5194/acp-8-7389-2008, 2008.

675 Duncan, B. N., Logan, J. a., Bey, I., Megretskaia, I. a., Yantosca, R. M., Novelli, P. C., Jones, N. B. and Rinsland, C. P.: Global budget of CO, 1988–1997: Source estimates and validation with a global model, *J. Geophys. Res.*, 112(D22), D22301, doi:10.1029/2007JD008459, 2007.

EPA: National Trends in CO Levels, Available from:  
<http://www.epa.gov/airtrends/carbon.html> (Accessed 12 February 2014).

680 Fisher, J. A., Wilson, S. R., Zeng, G., Williams, J. E., Emmons, L. K., Langenfelds, R. L., Krummel, P. B. and Steele, L. P.: Seasonal changes in the tropospheric carbon monoxide profile over the remote Southern Hemisphere evaluated using multi-model simulations and aircraft observations, *Atmos. Chem. Phys.*, 15(6), 3217–3239, doi:10.5194/acp-15-3217-

2015, 2015.

685 Folberth, G. A., Hauglustaine, D. A., Lathièrè, J. and Brocheton, F.: Interactive chemistry in the Laboratoire de Météorologie Dynamique general circulation model: model description and impact analysis of biogenic hydrocarbons on tropospheric chemistry, *Atmos. Chem. Phys.*, 6(8), 2273–2319, doi:10.5194/acp-6-2273-2006, 2006.

Folkins, I., Wennberg, P. O., Hanisco, T. F., Anderson, J. G. and Salawitch, R. J.: OH, HO<sub>2</sub>, and NO in two biomass burning plumes: Sources of HO<sub>x</sub> and implications for ozone production, *Geophys. Res. Lett.*, 24(24), 3185–3188, doi:10.1029/97GL03047, 1997.

690 Fortems-Cheiney, A., Chevallier, F., Pison, I., Bousquet, P., Carouge, C., Clerbaux, C., Coheur, P.-F., George, M., Hurtmans, D. and Szopa, S.: On the capability of IASI measurements to inform about CO surface emissions, *Atmos. Chem. Phys.*, 9(22), 8735–8743, 2009.

695 Fortems-Cheiney, A., Chevallier, F., Pison, I., Bousquet, P., Saunois, M., Szopa, S., Cressot, C., Kurosu, T. P., Chance, K. and Fried, A.: The formaldehyde budget as seen by a global-scale multi-constraint and multi-species inversion system, *Atmos. Chem. Phys.*, 12(15), 6699–6721, 2012.

700 Fortems-Cheiney, A., Chevallier, F., Pison, I., Bousquet, P., Szopa, S., Deeter, M. N. and Clerbaux, C.: Ten years of CO emissions as seen from Measurements of Pollution in the Troposphere (MOPITT), *J. Geophys. Res.*, 116(D5), doi:DOI: 10.1029/2010JD014416, 2011.

Giglio, L., Randerson, J. T. and van der Werf, G. R.: Analysis of daily, monthly, and annual burned area using the fourth-generation global fire emissions database (GFED4), *J. Geophys. Res. Biogeosciences*, 118(1), 317–328, doi:10.1002/jgrg.20042, 2013.

705 González Abad, G., Liu, X., Chance, K., Wang, H., Kurosu, T. P. and Suleiman, R.: Updated Smithsonian Astrophysical Observatory Ozone Monitoring Instrument (SAO OMI) formaldehyde retrieval, *Atmos. Meas. Tech.*, 8(1), 19–32, doi:10.5194/amt-8-19-2015, 2015.

710 Granier, C., Bessagnet, B., Bond, T., D'Angiola, A., Denier van der Gon, H., Frost, G. J., Heil, A., Kaiser, J. W., Kinne, S., Klimont, Z., Kloster, S., Lamarque, J.-F., Liousse, C., Masui, T., Meleux, F., Mieville, A., Ohara, T., Raut, J.-C., Riahi, K., Schultz, M. G., Smith, S. J., Thompson, A., Aardenne, J., Werf, G. R. and Vuuren, D. P.: Evolution of anthropogenic and biomass burning emissions of air pollutants at global and regional scales during the 1980–2010 period, *Clim. Change*, 109(1-2), 163–190, doi:10.1007/s10584-011-0154-1, 2011.

715 Hauglustaine, D. A.: Interactive chemistry in the Laboratoire de Météorologie Dynamique general circulation model: Description and background tropospheric chemistry evaluation, *J. Geophys. Res.*, 109(D4), D04314, doi:10.1029/2003JD003957, 2004.

Hauglustaine, D. A., Granier, C., Brasseur, G. P. and Mégie, G.: The importance of

- atmospheric chemistry in the calculation of radiative forcing on the climate system, *J. Geophys. Res.*, 99(D1), 1173, doi:10.1029/93JD02987, 1994.
- 720 Hofzumahaus, A., Rohrer, F., Lu, K., Bohn, B., Brauers, T., Chang, C.-C., Fuchs, H., Holland, F., Kita, K., Kondo, Y., Li, X., Lou, S., Shao, M., Zeng, L., Wahner, A. and Zhang, Y.: Amplified trace gas removal in the troposphere., *Science*, 324(5935), 1702–4, doi:10.1126/science.1164566, 2009.
- Holloway, T., Levy, H. and Kasibhatla, P.: Global distribution of carbon monoxide, *J. Geophys. Res.*, 105(D10), 12123, doi:10.1029/1999JD901173, 2000.
- 725 Hooghiemstra, P. B., Krol, M. C., Bergamaschi, P., de Laat, A. T. J., Van der Werf, G. R., Novelli, P. C., Deeter, M. N., Aben, I. and Röckmann, T.: Comparing optimized CO emission estimates using MOPITT or NOAA surface network observations, *J. Geophys. Res.*, 117(D6), doi:DOI: 10.1029/2011JD017043, 2012.
- 730 Hourdin, F., Musat, I., Bony, S., Braconnot, P., Codron, F., Dufresne, J.-L., Fairhead, L., Filiberti, M.-A., Friedlingstein, P., Grandpeix, J.-Y., Krinner, G., LeVan, P., Li, Z.-X. and Lott, F.: The LMDZ4 general circulation model: climate performance and sensitivity to parametrized physics with emphasis on tropical convection, *Clim. Dyn.*, 27(7-8), 787–813, doi:10.1007/s00382-006-0158-0, 2006.
- Jacob, D.: Introduction to atmospheric chemistry, Princeton University Press., 1999.
- 735 Jiang, Z., Jones, D. B. a., Worden, H. M., Deeter, M. N., Henze, D. K., Worden, J., Bowman, K. W., Brenninkmeijer, C. a. M. and Schuck, T. J.: Impact of model errors in convective transport on CO source estimates inferred from MOPITT CO retrievals, *J. Geophys. Res. Atmos.*, 118(4), 2073–2083, doi:10.1002/jgrd.50216, 2013.
- 740 Khalil, M. A. K. and Rasmussen, R. A.: Carbon monoxide in the Earth's atmosphere: indications of a global increase, *Nature*, 332(6161), 242–245, 1988.
- Kim, D.-H., Sexton, J. O. and Townshend, J. R.: Accelerated Deforestation in the Humid Tropics from the 1990s to the 2000s, *Geophys. Res. Lett.*, doi:10.1002/2014GL062777, 2015.
- 745 Kopacz, M., Jacob, D. J., Fisher, J. A., Logan, J. A., Zhang, L., Megretskaia, I. A., Yantosca, R. M., Singh, K., Henze, D. K., Burrows, J. P., Buchwitz, M., Khlystova, I., McMillan, W. W., Gille, J. C., Edwards, D. P., Eldering, A., Thouret, V. and Nedelec, P.: Global estimates of CO sources with high resolution by adjoint inversion of multiple satellite datasets (MOPITT, AIRS, SCIAMACHY, TES), *Atmos. Chem. Phys.*, 10(3), 855–876, doi:10.5194/acp-10-855-2010, 2010.
- 750 Kurokawa, J., Ohara, T., Morikawa, T., Hanayama, S., Janssens-Maenhout, G., Fukui, T., Kawashima, K. and Akimoto, H.: Emissions of air pollutants and greenhouse gases over Asian regions during 2000–2008: Regional Emission inventory in ASia (REAS) version 2,

Atmos. Chem. Phys., 13(21), 11019–11058, doi:10.5194/acp-13-11019-2013, 2013.

755 Lamarque, J. F., Bond, T. C., Eyring, V., Granier, C., Heil, A., Klimont, Z., Lee, D., Liousse, C., Mieville, A., Owen, B., Schultz, M. G., Shindell, D., Smith, S. J., Stehfest, E., Van Aardenne, J., Cooper, O. R., Kainuma, M., Mahowald, N., McConnell, J. R., Naik, V., Riahi, K. and van Vuuren, D. P.: Historical (1850–2000) gridded anthropogenic and biomass burning emissions of reactive gases and aerosols: methodology and application, Atmos. Chem. Phys., 10(15), 7017–7039, 2010.

760 van Leeuwen, T. T., Peters, W., Krol, M. C. and van der Werf, G. R.: Dynamic biomass burning emission factors and their impact on atmospheric CO mixing ratios, J. Geophys. Res. Atmos., 118(12), 6797–6815, doi:10.1002/jgrd.50478, 2013.

765 Lelieveld, J., Butler, T. M., Crowley, J. N., Dillon, T. J., Fischer, H., Ganzeveld, L., Harder, H., Lawrence, M. G., Martinez, M., Taraborrelli, D. and Williams, J.: Atmospheric oxidation capacity sustained by a tropical forest., Nature, 452(7188), 737–40, doi:10.1038/nature06870, 2008.

Li, L. and Liu, Y.: Space-borne and ground observations of the characteristics of CO pollution in Beijing, 2000–2010, Atmos. Environ., 45(14), 2367–2372, doi:10.1016/j.atmosenv.2011.02.026, 2011.

770 Logan, J. A., Prather, M. J., Wofsy, S. C. and McElroy, M. B.: Tropospheric Chemistry: A Global Perspective, J. Geophys. Res., (86), 1–45, doi:DOI: 10.1029/JC086iC08p07210, 1981.

775 Mao, J., Ren, X., Zhang, L., Van Duin, D. M., Cohen, R. C., Park, J.-H., Goldstein, A. H., Paulot, F., Beaver, M. R., Crouse, J. D., Wennberg, P. O., DiGangi, J. P., Henry, S. B., Keutsch, F. N., Park, C., Schade, G. W., Wolfe, G. M., Thornton, J. A. and Brune, W. H.: Insights into hydroxyl measurements and atmospheric oxidation in a California forest, Atmos. Chem. Phys., 12(17), 8009–8020, doi:10.5194/acp-12-8009-2012, 2012.

Meyfroidt, P. and Lambin, E. F.: Global Forest Transition: Prospects for an End to Deforestation, Annu. Rev. Environ. Resour., 36(1), 343–371, doi:10.1146/annurev-environ-090710-143732, 2011.

780 Mu, M., Randerson, J. T., van der Werf, G. R., Giglio, L., Kasibhatla, P., Morton, D., Collatz, G. J., DeFries, R. S., Hyer, E. J., Prins, E. M., Griffith, D. W. T., Wunch, D., Toon, G. C., Sherlock, V. and Wennberg, P. O.: Daily and 3-hourly variability in global fire emissions and consequences for atmospheric model predictions of carbon monoxide, J. Geophys. Res. Atmos., 116(D24), doi:10.1029/2011JD016245, 2011.

785 Naik, V., Voulgarakis, A., Fiore, A. M., Horowitz, L. W., Lamarque, J.-F., Lin, M., Prather, M. J., Young, P. J., Bergmann, D., Cameron-Smith, P. J., Cionni, I., Collins, W. J., Dalsøren, S. B., Doherty, R., Eyring, V., Faluvegi, G., Folberth, G. A., Josse, B., Lee, Y. H., MacKenzie, I. A., Nagashima, T., van Noije, T. P. C., Plummer, D. A., Righi, M., Rumbold,

- 790 S. T., Skeie, R., Shindell, D. T., Stevenson, D. S., Strode, S., Sudo, K., Szopa, S. and Zeng, G.: Preindustrial to present-day changes in tropospheric hydroxyl radical and methane lifetime from the Atmospheric Chemistry and Climate Model Intercomparison Project (ACCMIP), *Atmos. Chem. Phys.*, 13(10), 5277–5298, doi:10.5194/acp-13-5277-2013, 2013.
- Novelli, P. C., Masarie, K. A., Lang, P. M., Hall, B. D., Myers, R. C. and Elkins, J. W.: Reanalysis of tropospheric CO trends: Effects of the 1997–1998 wildfires, *J. Geophys. Res. Atmos.*, 108(D15), 4464, doi:10.1029/2002JD003031, 2003.
- 795 Patra, P. K., Houweling, S., Krol, M., Bousquet, P., Belikov, D., Bergmann, D., Bian, H., Cameron-Smith, P., Chipperfield, M. P., Corbin, K., Fortems-Cheiney, A., Fraser, A., Gloor, E., Hess, P., Ito, A., Kawa, S. R., Law, R. M., Loh, Z., Maksyutov, S., Meng, L., Palmer, P. I., Prinn, R. G., Rigby, M., Saito, R. and Wilson, C.: TransCom model simulations of CH<sub>4</sub> and related species: linking transport, surface flux and chemical loss with CH<sub>4</sub> variability in the troposphere and lower stratosphere, *Atmos. Chem. Phys.*, 11(24), 12813–12837, doi:10.5194/acp-11-12813-2011, 2011.
- 800 Pétron, G.: Inverse modeling of carbon monoxide surface emissions using Climate Monitoring and Diagnostics Laboratory network observations, *J. Geophys. Res.*, 107(D24), 4761, doi:10.1029/2001JD001305, 2002.
- 805 Pétron, G., Granier, C., Khattatov, B., Yudin, V., Lamarque, J.-F., Emmons, L., Gille, J. and Edwards, D. P.: Monthly CO surface sources inventory based on the 2000–2001 MOPITT satellite data, *Geophys. Res. Lett.*, 31(21), L21107, doi:10.1029/2004GL020560, 2004.
- Pison, I., Bousquet, P., Chevallier, F., Szopa, S. and Hauglustaine, D.: Multi-species inversion of CH<sub>4</sub>, CO and H<sub>2</sub> emissions from surface measurements, *Atmos. Chem. Phys.*, 9(14), 5281–5297, doi:10.5194/acp-9-5281-2009, 2009.
- 810 Poulter, B., Frank, D., Ciais, P., Myneni, R. B., Andela, N., Bi, J., Broquet, G., Canadell, J. G., Chevallier, F., Liu, Y. Y., Running, S. W., Sitch, S. and van der Werf, G. R.: Contribution of semi-arid ecosystems to interannual variability of the global carbon cycle, *Nature*, 509(7502), 600–603, doi:10.1038/nature13376, 2014.
- 815 Randerson, J. T., Chen, Y., van der Werf, G. R., Rogers, B. M. and Morton, D. C.: Global burned area and biomass burning emissions from small fires, *J. Geophys. Res.*, 117(G4), G04012, doi:10.1029/2012JG002128, 2012.
- Rayner, P. J. and O’Brien, D. M.: The utility of remotely sensed CO<sub>2</sub> concentration data in surface source inversions, *Geophys. Res. Lett.*, 28(1), 175–178, doi:10.1029/2000GL011912, 2001.
- 820 Reuter, M., Buchwitz, M., Hilboll, A., Richter, A., Schneising, O., Hilker, M., Heymann, J., Bovensmann, H. and Burrows, J. P.: Decreasing emissions of NO<sub>x</sub> relative to CO<sub>2</sub> in East Asia inferred from satellite observations, *Nat. Geosci.*, 7, doi:10.1038/ngeo2257, 2014.

- 825 Rohrer, F., Lu, K., Hofzumahaus, A., Bohn, B., Brauers, T., Chang, C.-C., Fuchs, H., Häsel, R., Holland, F., Hu, M., Kita, K., Kondo, Y., Li, X., Lou, S., Oebel, A., Shao, M., Zeng, L., Zhu, T., Zhang, Y. and Wahner, A.: Maximum efficiency in the hydroxyl-radical-based self-cleansing of the troposphere, *Nat. Geosci.*, 7(8), 559–563, doi:10.1038/ngeo2199, 2014.
- 830 Shindell, D. T., Faluvegi, G., Stevenson, D. S., Krol, M. C., Emmons, L. K., Lamarque, J.-F., Pétron, G., Dentener, F. J., Ellingsen, K., Schultz, M. G., Wild, O., Amann, M., Atherton, C. S., Bergmann, D. J., Bey, I., Butler, T., Cofala, J., Collins, W. J., Derwent, R. G., Doherty, R. M., Drevet, J., Eskes, H. J., Fiore, A. M., Gauss, M., Hauglustaine, D. A., Horowitz, L. W., Isaksen, I. S. A., Lawrence, M. G., Montanaro, V., Müller, J.-F., Pitari, G., Prather, M. J., Pyle, J. A., Rast, S., Rodriguez, J. M., Sanderson, M. G., Savage, N. H., Strahan, S. E., Sudo, K., Szopa, S., Unger, N., van Noije, T. P. C., Zeng, G., G, F. and D S, S.: Multimodel  
835 simulations of carbon monoxide: Comparison with observations and projected near-future changes, *J. Geophys. Res.*, 111(D19), D19306, doi:10.1029/2006JD007100, 2006.
- De Smedt, I., Stavrou, T., Müller, J.-F., van der A, R. J. and Van Roozendaal, M.: Trend detection in satellite observations of formaldehyde tropospheric columns, *Geophys. Res. Lett.*, 37(18), doi:10.1029/2010GL044245, 2010.
- 840 Stavrou, T. and Müller, J.-F.: Grid-based versus big region approach for inverting CO emissions using Measurement of Pollution in the Troposphere (MOPITT) data, *J. Geophys. Res.*, 111(D15), D15304, doi:10.1029/2005JD006896, 2006.
- 845 Stein, O., Schultz, M. G., Bouarar, I., Clark, H., Huijnen, V., Gaudel, A., George, M. and Clerbaux, C.: On the wintertime low bias of Northern Hemisphere carbon monoxide found in global model simulations, *Atmos. Chem. Phys.*, 14(17), 9295–9316, doi:10.5194/acp-14-9295-2014, 2014.
- 850 Stocker, T. F., Qin, D., Plattner, G.-K., Tignor, M., Allen, S. K., Boschung, J., Nauels, A., Xia, Y., Bex, V., Midgley, P. M. and others: Climate Change 2013. The Physical Science Basis. Working Group I Contribution to the Fifth Assessment Report of the Intergovernmental Panel on Climate Change-Abstract for decision-makers., 2013.
- Thompson, A. M.: The Oxidizing Capacity of the Earth's Atmosphere: Probable Past and Future Changes, *Science* (80), 256(5060), 1157–1165, doi:10.1126/science.256.5060.1157, 1992.
- 855 Tohjima, Y., Kubo, M., Minejima, C., Mukai, H., Tanimoto, H., Ganshin, A., Maksyutov, S., Katsumata, K., Machida, T. and Kita, K.: Temporal changes in the emissions of CH<sub>4</sub> and CO from China estimated from CH<sub>4</sub>/CO<sub>2</sub> and CO/CO<sub>2</sub> correlations observed at Hateruma Island, *Atmos. Chem. Phys.*, 14(3), 1663–1677, doi:10.5194/acp-14-1663-2014, 2014.
- 860 Wang, R., Tao, S., Shen, H., Huang, Y., Chen, H., Balkanski, Y., Boucher, O., Ciais, P., Shen, G., Li, W., Zhang, Y., Chen, Y., Lin, N., Su, S., Li, B., Liu, J. and Liu, W.: Trend in global black carbon emissions from 1960 to 2007., *Environ. Sci. Technol.*, 48(12), 6780–7,

doi:10.1021/es5021422, 2014.

Warner, J., Carminati, F., Wei, Z., Lahoz, W. and Attié, J.-L.: Tropospheric carbon monoxide variability from AIRS under clear and cloudy conditions, *Atmos. Chem. Phys.*, 13(24), 12469–12479, doi:10.5194/acp-13-12469-2013, 2013.

865 van der Werf, G. R., Randerson, J. T., Giglio, L., Collatz, G. J., Kasibhatla, P. S. and Arellano, A. F.: Interannual variability in global biomass burning emissions from 1997 to 2004, *Atmos. Chem. Phys.*, 6(11), 3423–3441, doi:10.5194/acp-6-3423-2006, 2006.

870 Van der Werf, G. R., Randerson, J. T., Giglio, L., Collatz, G. J., Mu, M., Kasibhatla, P. S., Morton, D. C., DeFries, R. S., Jin, Y. and van Leeuwen, T. T.: Global fire emissions and the contribution of deforestation, savanna, forest, agricultural, and peat fires (1997–2009), *Atmos. Chem. Phys.*, 10(23), 11707–11735, 2010.

875 Worden, H. M., Deeter, M. N., Frankenberg, C., George, M., Nichitiu, F., Worden, J., Aben, I., Bowman, K. W., Clerbaux, C., Coheur, P.-F., de Laat, A. T. J., Detweiler, R., Drummond, J. R., Edwards, D. P., Gille, J. C., Hurtmans, D., Luo, M., Martínez-Alonso, S., Massie, S., Pfister, G. and Warner, J. X.: Decadal record of satellite carbon monoxide observations, *Atmos. Chem. Phys.*, 13(2), 837–850, 2013.

Yevich, R. and Logan, J. A.: An assessment of biofuel use and burning of agricultural waste in the developing world, *Global Biogeochem. Cycles*, 17(4), doi:10.1029/2002GB001952, 2003.

880 Yoon, J. and Pozzer, A.: Model-simulated trend of surface carbon monoxide for the 2001–2010 decade, *Atmos. Chem. Phys.*, 14(19), 10465–10482, doi:10.5194/acp-14-10465-2014, 2014.

885 Zellweger, C., Hüglin, C., Klausen, J., Steinbacher, M., Vollmer, M. and Buchmann, B.: Inter-comparison of four different carbon monoxide measurement techniques and evaluation of the long-term carbon monoxide time series of Jungfraujoch, *Atmos. Chem. Phys.*, 9(11), 3491–3503, doi:10.5194/acp-9-3491-2009, 2009.

## Tables

**Table 1. Prior datasets for the sources and sinks of CO.** Mean annual sums are calculated for the period from 2002 to 2011. The global annual prior error budgets are reported with TransCom-OH field.

5

	Sectors	Mean Annual Sum (Tg yr <sup>-1</sup> )	Dataset/ Model	References
	<b>Sources:</b>			
	Biomass burning	327	GFEDv3.1	Van der Werf et al., 2010
	Anthropogenic Emissions	588	MACCity	Lamarque et al., 2010
	Ocean	54	PISCES	Updated from Aumont et al. 2006
	<b><i>Sum of surface emissions</i></b>	<b>969±180</b> <sup>(1)</sup>		
<b>CO</b>	Oxidation from NMVOC	335±43 <sup>(2)</sup>	LMDz-INCA	Folberth et al. 2006
	Oxidation from CH <sub>4</sub>	885±92 <sup>(3)</sup>		
	<b><i>Sum of chemical sources</i></b>	<b>1220</b>		
	<b>Sinks:</b>			
	Oxidation by OH	<b>2197</b>	TransCom-OH	Patra et al. 2011

(1) The uncertainty represents the SD of the global annual error budgets in the prior CO emissions in the inversion configuration.

(2) The SD is calculated into the equivalent CO amount from global annual error budgets of the pre-calculated CH<sub>2</sub>O production fields.

(3) The SD is calculated into the equivalent CO amount from global annual error budgets of the prior CH<sub>4</sub> emissions assuming they are all oxidized into CO in a single step. The prior CH<sub>4</sub> emission (506 TgCO yr<sup>-1</sup>) datasets are detailed in Cressot et al. (2014).

10

15

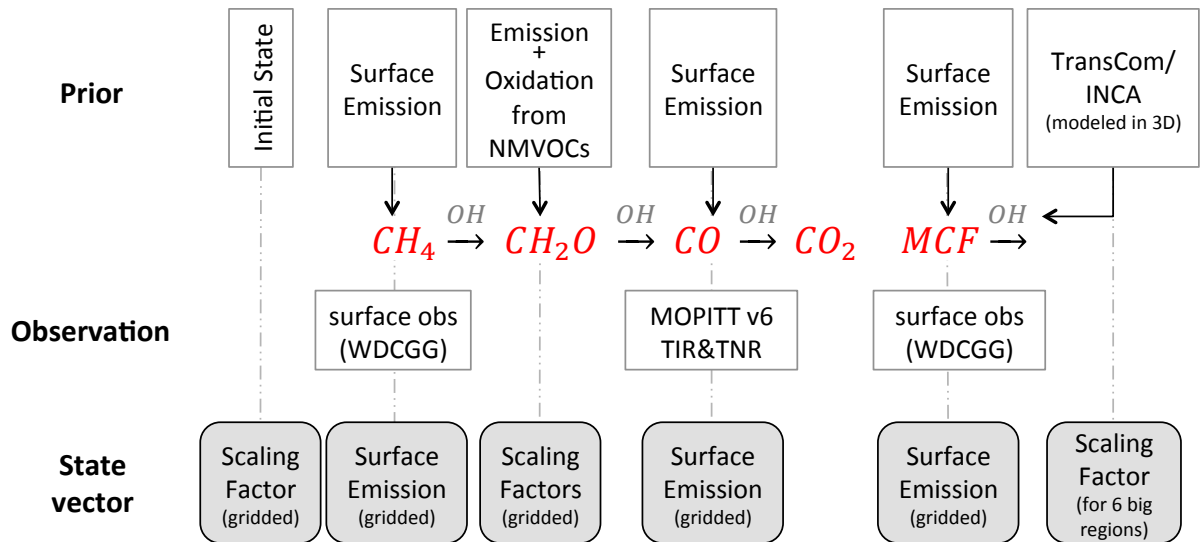


**Table 3. Fitness of CH<sub>4</sub> and MCF observations assimilated in the inversion.**

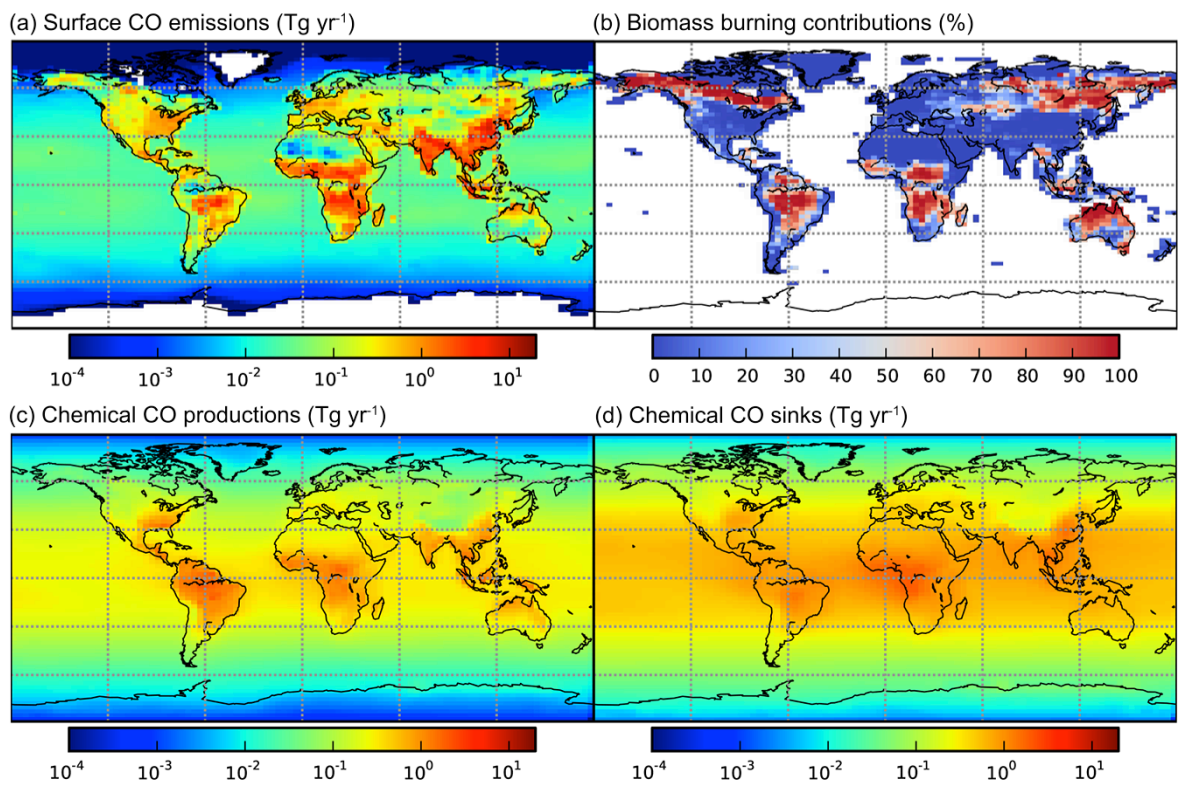
Region	OH-type	CH <sub>4</sub> (ppb)				MCF (ppt)			
		Mean bias		Residual square		Mean bias		Residual square	
		<i>prior</i>	<i>posterior</i>	<i>prior</i>	<i>posterior</i>	<i>prior</i>	<i>posterior</i>	<i>prior</i>	<i>posterior</i>
<b>NH(30-90)</b>	<i>TransCom</i>	20.6	2.4	749.6	22.2	1.02	-0.02	1.14	0.05
	<i>INCA</i>	-21.0	2.5	658.1	20.1	0.44	-0.09	0.28	0.07
<b>NH(0-30)</b>	<i>TransCom</i>	15.8	1.5	452.6	19.1	0.90	-0.20	0.91	0.16
	<i>INCA</i>	-21.1	-0.1	564.9	13.9	0.40	-0.20	0.21	0.11
<b>SH(0-30)</b>	<i>TransCom</i>	10.9	-2.4	222.1	20.1	1.19	0.09	1.61	0.13
	<i>INCA</i>	-14.3	-4.0	264.9	29.5	0.88	0.23	0.94	0.15
<b>SH(30-90)</b>	<i>TransCom</i>	14.4	0.2	308.3	4.7	0.88	-0.24	0.90	0.17
	<i>INCA</i>	-7.9	-0.4	96.6	5.7	0.60	-0.06	0.46	0.07

# Figures

Fig. 1. Schematics of the input information provided to the inversion and of the inversion state vector.



35 **Fig. 2. Distribution of prior budget terms for CO.** Annual mean values per model grid ( $2.5^\circ$  latitude  $\times$   $3.75^\circ$  longitude) from 2002 to 2011 are shown. (a) Surface CO emissions, (b) Relative percentages of CO emissions from biomass burning over land, (c) Atmospheric CO productions from  $\text{CH}_4$  and NMVOCs, (d) Atmospheric CO chemical sinks. The chemical productions and sinks are calculated with TransCom-OH.



40 **Fig. 3. Spatial and vertical distribution of OH concentrations in TransCom, INCA and their relative differences.** The TransCom OH is interpolated from its original 60 pressure levels into the LMDz 19 eta- pressure levels.

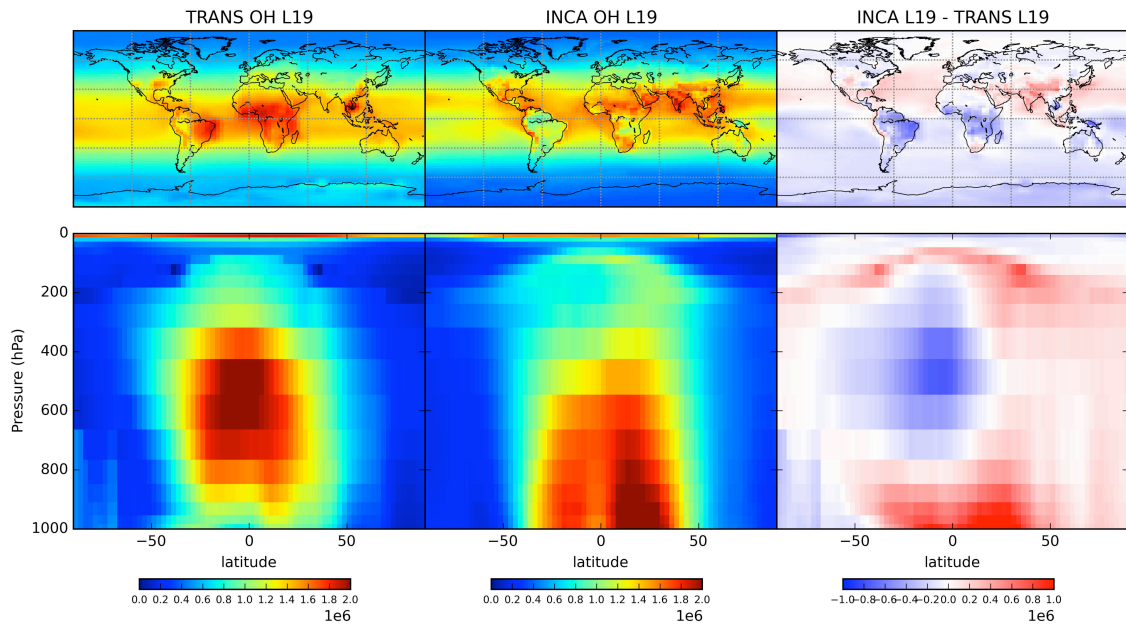
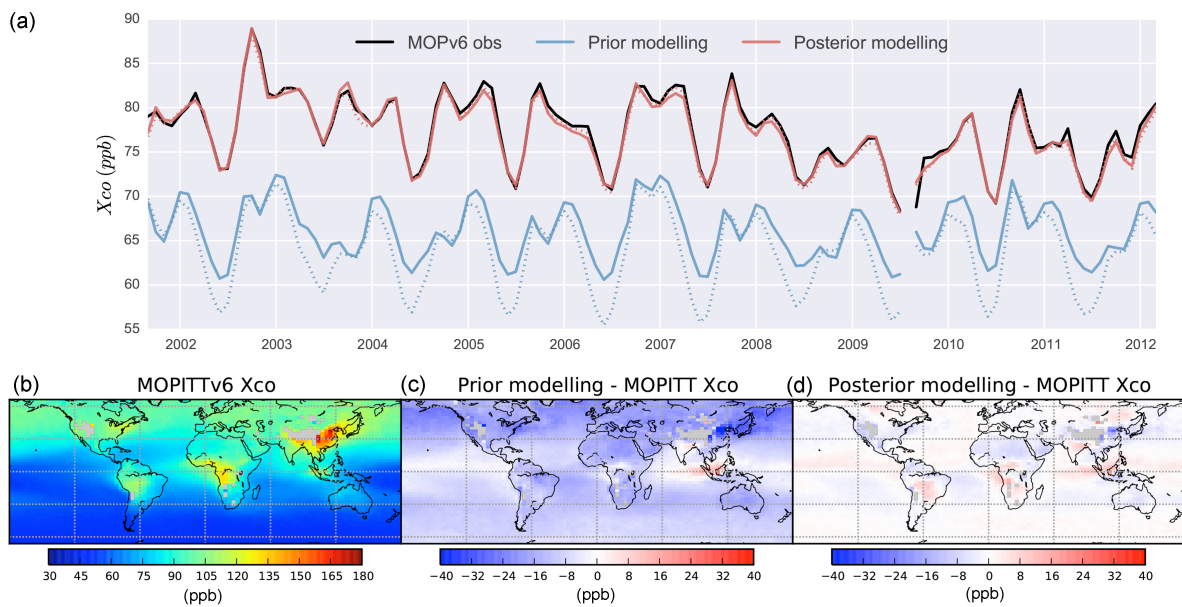
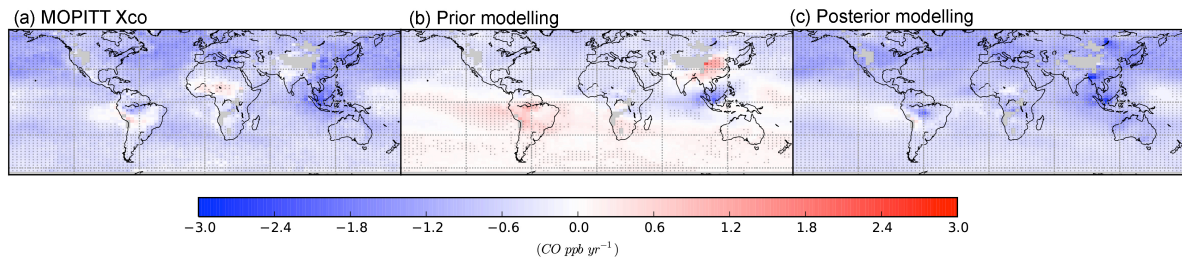


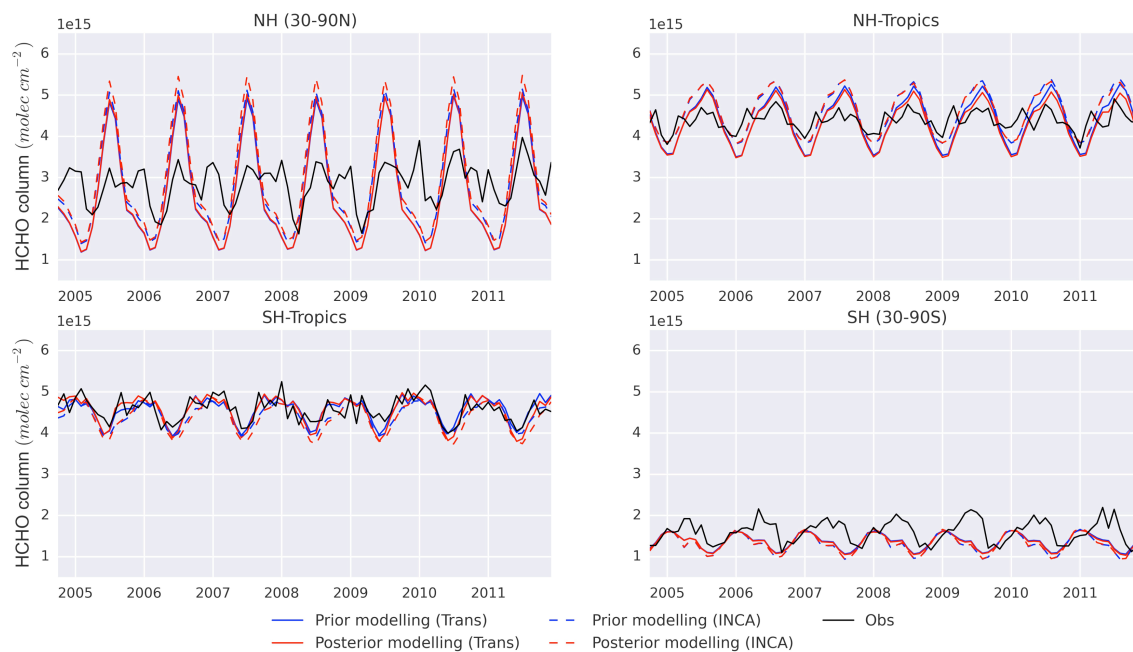
**Fig. 4. Time series and spatial distributions of CO total column ( $X_{CO}$ ).** (a) Time series of global monthly mean mole fraction in CO column. The black line represents satellite observation of MOPITTv6  $X_{CO}$ , the blue (red) lines represent the prior (posterior)  $X_{CO}$  retrievals. Solid lines represent the results with TransCom-OH, and dotted lines represent results with INCA-OH. (b) Distribution of multi-year mean annual  $X_{CO}$  of MOPITTv6 retrieval. (c) Mean annual difference between the prior  $X_{CO}$  and MOPITT  $X_{CO}$ . (d) Mean annual difference between the posterior  $X_{CO}$  and MOPITT  $X_{CO}$ . Simulations shown in c and d used TransCom-OH. The results with INCA-OH are of similar spatial distributions and are not shown here.



55 **Fig. 5. Distribution of  $X_{CO}$  trends from 2002 to 2011 in (a) MOPITTv6 retrievals, (b) the prior simulation and (c) the posterior simulation. Black crosses indicate significance at 95% confidence level.**

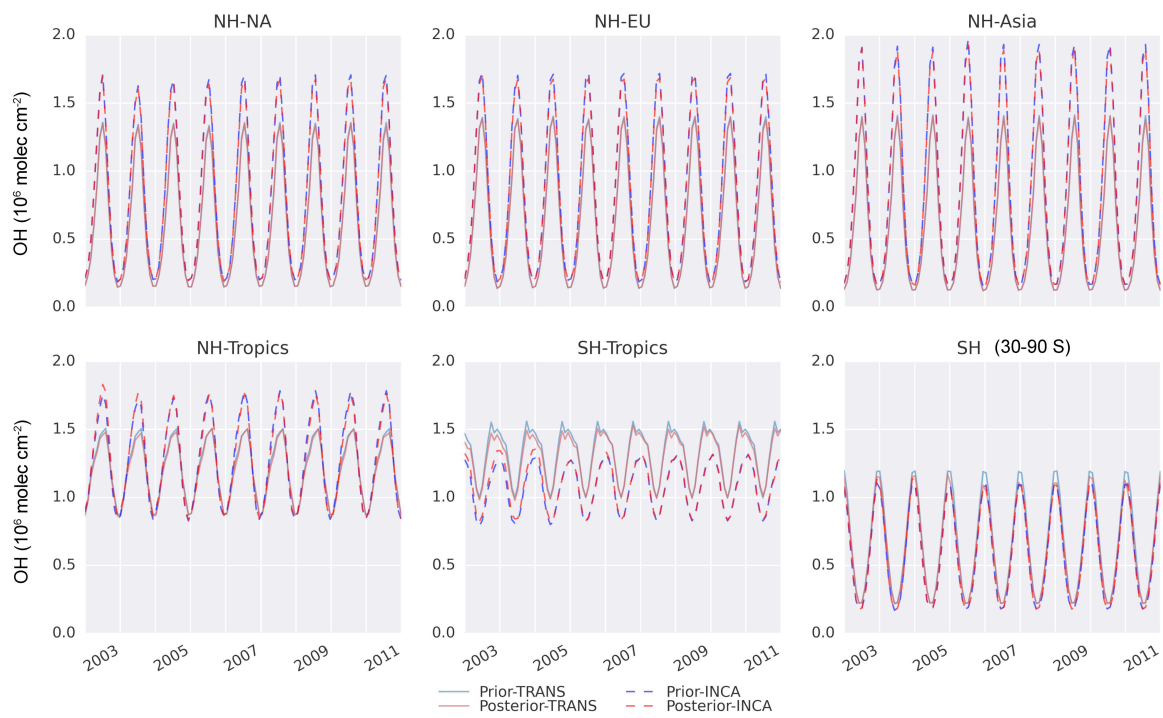


60 **Fig. 6. Time series of CH<sub>2</sub>O total column averaged by latitudinal bands.** The black lines indicate the CH<sub>2</sub>O total column from SAO OMI retrievals, blue lines indicate prior simulations, and red lines indicate posterior simulations. Solid lines represent TransCom-OH, and dashed lines represent INCA-OH.



65

**Fig. 7. Column mean OH concentrations in the prior and posterior.** The results are shown for the 6 big regions over which OH is optimized.



75 **Fig. 8. Time series of global mean annual CO budget changes from 2002 to 2011.** Each  
 component is shown in a different colour. Solid lines indicate the prior values (mean values of the two  
 OH fields are shown for the prior chemical CO production and sink). Dash-dot lines indicate posterior  
 with TransCom-OH and dotted lines represent posterior with INCA-OH. With the order from left to  
 80 are denotes successively if the trend is statistically significant. \* denotes 95% confidence level and \*\*  
 denotes 99% confidence level.

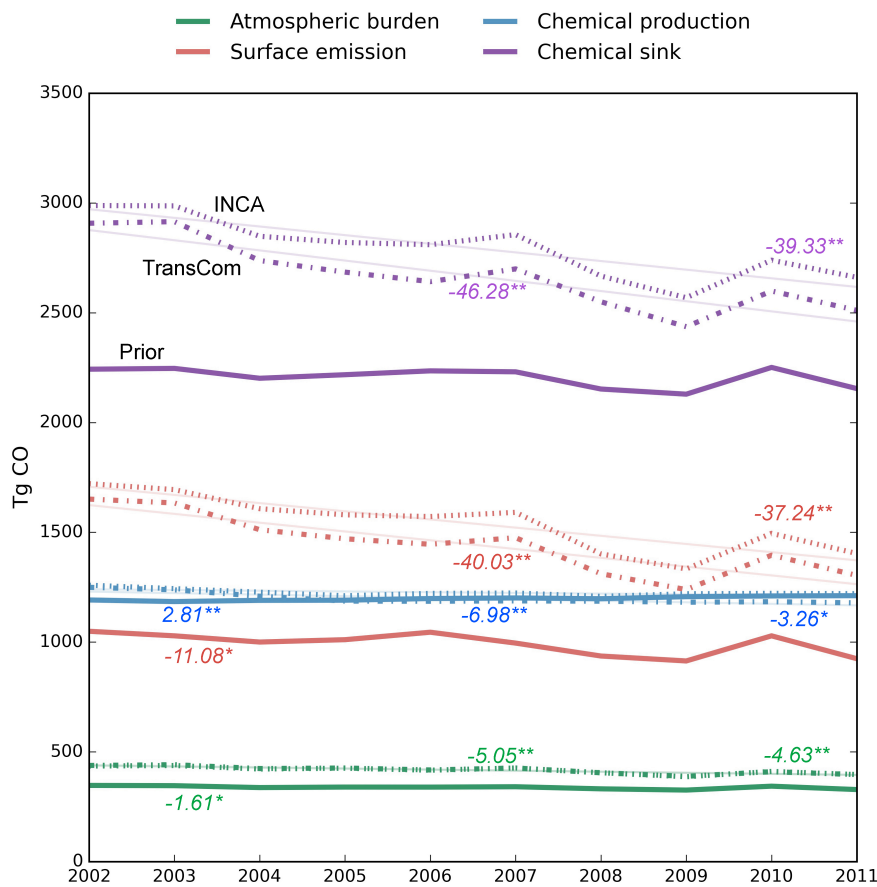


**Fig. 9. Trends distributions of CO surface emissions in the prior and in the posterior from 2002 to 2011.**

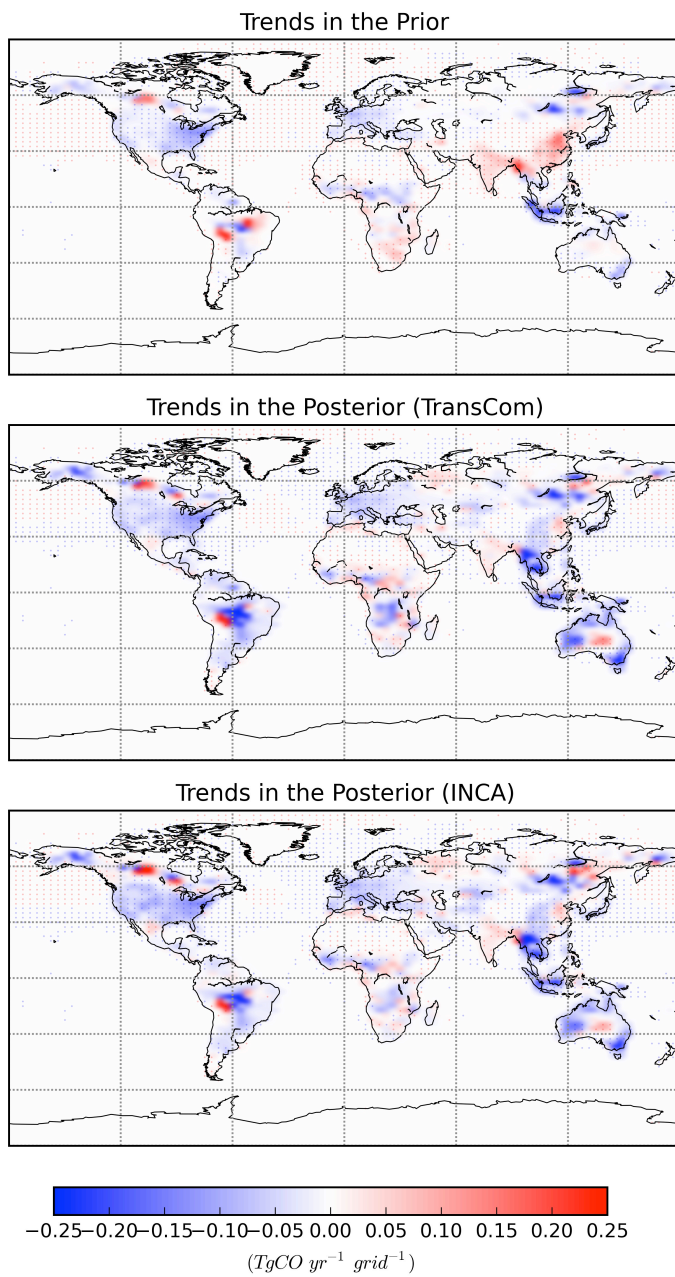


**Fig. 10. Annual prior (blue) and posterior (red) CO emissions in each sub-region from 2002 to 2011.** The dash lines represent linear regressions, beside which  $s$  denotes the linear slope and  $p$  denotes the p-value for the regression. The notation for the sub-regions are listed as follows and the extent of each region is shown in Fig. A1. BOAS - Boreal Asia, BONA - Boreal North America, USA - USA, WSEU – West Europe, ESEU – East Europe, MIDE – Middle East, SCAS – South Central Asia, SEAS – South East Asia, INDO- Indonesia, AUST – Australia, NHSA- North Hemisphere South America, SHSA - South Hemisphere South America, NHAf - North Hemisphere Africa, SHAF – South Hemisphere Africa, OCEAN – all ocean emissions both biogenic and anthropogenic emissions.

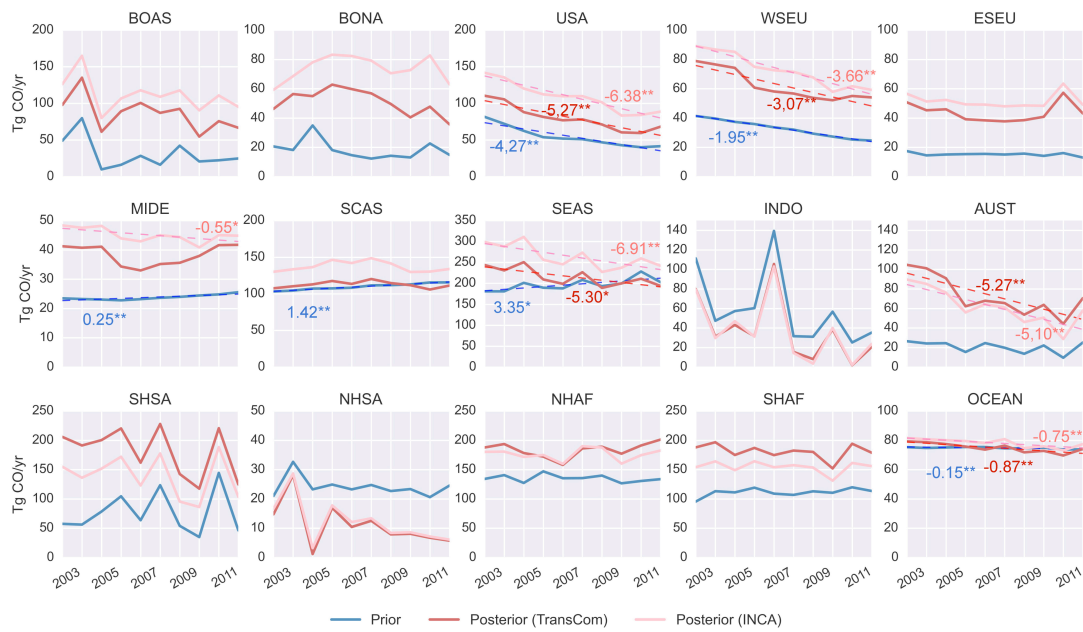


Fig. A1. Sub-region extent.

